CHAPTER 4
CONFINED FLAT–PLATEN UNIAXIAL COMPRESSION EXPERIMENTS

This chapter documents the confined flat–platen uniaxial compression experiments conducted as part of this investigation. Confined flat-platen uniaxial compression experiments provide a simple loading scenario for determination of suitable image measurement parameters and nodal density for ITA analysis of prepared cane and bagasse. Time series of digital images were captured for all experiments, forming the basis for numerical image analysis. The first series of experiments (termed herein as the *sighting trials*) involved two prepared cane and two final bagasse experiments, providing local fibre deformation data over a wide range of material compaction. Material inhomogeneity was encountered in the sighting trials as a direct result of the particle size distribution and the physical testing procedure employed. A subsequent series of final bagasse experiments (termed herein as the *auxiliary trials*) were thus conducted in an attempt to eliminate these difficulties. Experimental techniques were refined and repeat experiments were conducted for both final bagasse and a sieved product of final bagasse, referred to herein as *fines*.

The image acquisition system and ITA software were also employed in an ancillary investigation into bagasse behaviour during uniaxial compression between grooved surfaces (Kauppila et al. 2003). Video footage was taken for a series of uniaxial grooving tests, and was utilised as a means for qualifying the nature of blanket/groove interactions. The ITA software was applied to suitable tests in order to gain insight into juice flow through the blanket. A brief overview of the role that ITA played in this ancillary work is presented in Section 4.3.

4.1 The sighting trials

The sighting trials involved two prepared cane and two final bagasse experiments, providing local fibre deformation data over a wide range of compaction, for a simple one dimensional loading scenario. Clean whole stick sugar cane (Q96) was sourced from a farm in the Burdekin district, and final bagasse was collected from the final mill on the A-side milling train at Invicta sugar-mill.

4.1.1 Aims and scope of the experimental program

The aims of the experimental program are to:

1. Collect visual data for image measurement analysis.
2. Determine suitable nodal density and image measurement parameter values for image measurement analysis of prepared cane and bagasse.
3. Measure the two–dimensional local fibre deformation field for each material sample.
4. Assess the homogeneity of prepared cane and bagasse under simple confined one-dimensional loading.

Experimental program scope:

1. All prepared cane experiments were conducted using one variety of cane and one preparation level.
2. All final bagasse experiments were conducted using material from the same sample of bagasse taken from Invicta mill.
3. Image data was collected for all experiments.
4. Juice extraction was given no consideration.

4.1.2 Apparatus

Cane was prepared in the SRI laboratory shredder (Figure 4.1(a)) at 2000 revolutions per minute at James Cook University. The fibre content of the cane and bagasse was measured using the SRI fibre determination apparatus (Anon. 1991), shown below in Figure 4.1(b).

Figure 4.1. (a) SRI hammer shredder. (b) SRI fibre determination apparatus.

The uniaxial cell (Figure 4.2) used for the compression experiments comprised of two non-porous end plates, one porous side-plate and a non-porous glass *viewing window*. The flat platens were also porous. A leather seal was employed on the viewing side of each platen. The cell cross-sectional area (98 mm x 228 mm) is concurrent with that used in previous uniaxial work (Murry 1960, Loughran 1990, Adam 1997).

Figure 4.2. Confined uniaxial compression cell.

The tests were performed in the 1000kN MTS hydraulic testing apparatus shown in Figure 4.3. The MTS load ram has a maximum travel of 130 mm and a maximum velocity of 10 mm/s. The MTS headstock is equipped with a 1000 kN load cell and a LVDT providing force and displacement output.

Figure 4.3. MTS hydraulic testing apparatus.

The CCD unit (Sony DCR-TRV900) was mounted on a solid steel base approximately 1600 mm from the MTS centre. This was done in order to achieve a telescopic focal plane for image capture. The CCD was connected to an Apple I-mac Computer via an IEEE 1394 connection. Imovie2 frame grabbing software was employed for the capture of video footage. A light shroud was erected around the CCD and MTS machine in order to eliminate reflections from the surroundings (Figure 4.4). Samples were illuminated by a two–thousand Watt studio light mounted on a tripod.

Figure 4.4. MTS testing arrangement.

4.1.3 Procedure

The cane used in the experiment was variety Q96, grown near Giru. Cane stalks were cut and cleaned and promptly delivered to a cold room for storage at -4°C. The experiment was conducted within 48 hours of the cane being stored. Twenty stalks of cane were prepared in the SRI hammer shredder at 2000 revolutions per minute and mixed thoroughly (Anon. 1991). A two-kilogram sub–sample was taken and two 500 gram portions were placed in the SRI fibre determination apparatus. Results of the fibre tests are shown in Table 4.1.

Sample #	1	2
Initial can mass [g]	1312.2	1300.7
Initial prepared cane mass [g]	500	500
Mass out 1 [g]	1401.0	1390.3
Mass out 2 [g]	1401.0	1390.3
Mass of hot dry can [g]	1320.3	1308.7
Fibre mass [g]	80.7	81.6
Fibre content	0.1614	0.1632
Average fibre content	0.1623	

Table 4.1. Prepared cane (Q96 variety) mass fraction fibre content analysis.

Final bagasse was collected from the last mill on the A-side milling train at Invicta mill and stored at -4°C. All bagasse tests were conducted using material from one container of collected bagasse. The bagasse was thoroughly mixed (Anon. 1991) and two 200 gram samples were taken for fibre determination. The results of the fibre tests are shown in Table 4.2.

Sample #	1	2
Initial can mass [g]	1312.2	1300.7
Initial bagasse mass [g]	200	200
Mass out 1 [g]	1428.5	1416.6
Mass out 2 [g]	1428.5	1416.6
Mass of hot dry can [g]	1320.2	1308.7
Fibre mass [g]	108.3	107.9
Fibre content	0.5415	0.5395
Average fibre content	0.5405	

Table 4.2. Invicta mill final mill bagasse mass fraction fibre content analysis.

Material seed was prepared by sieving fifteen kilograms of bagasse through a sieve stack containing three sieve sizes (11 mm, 7 mm, 2.5 mm). The material from the 2.5 mm aperture sieve was dyed black and dried. Fifty grams of material seed was thoroughly mixed with each experimental sample. This amount was determined

volumetrically to provide sufficient contrasting pixels in each sub–region in the plane of view. The material seed is shown in Figure 4.5.

Figure 4.5. Material seed for experimental samples.

Material samples were loaded into the top of the cell as evenly as possible. The cell was then lifted onto the MTS ram and enclosed in the light shroud. The headstock was utilised to pre–compress each sample to an initial height of 165 mm. Each sample was then compressed at a constant velocity of 2 mm/s (considered small enough to avoid strain rate dependent behaviour due to juice pressure in the prepared cane samples) to a final height of 55 mm. The samples were then held at the final height for 15 seconds. Load and displacement data were recorded and stored in data files corresponding to each experiment.

4.1.4 Experimental program

The experimental program aimed to capture image data over a wide range of compaction for both prepared cane of nominal factory preparation and final mill bagasse. Two experiments for each material were conducted giving a total of four experiments. For each material considered, the large sample mass (PC_high and FB_high in Table 4.3) was such that the fibre density (compaction) was 500 kg/m^3 at a final blanket height of 55 mm. The small sample mass (PC_low and FB_low in Table 4.3) was then determined, such that the final compaction (final blanket height of 55 mm) was equal to the initial compaction of the large material sample. The sample parameters are shown in Table 4.3.

Test #	Descript.	Material fibre content	Material mass [kg]	Seed fibre content	Seed mass [kg]	Sample fibre content	Sample mass [kg]
1	PC_High	0.162	3.6645	0.7	0.05	0.170	3.7145
2	PC_Low	0.162	1.0777	0.7	0.05	0.186	1.1277
3	FB_High	0.541	1.1004	0.7	0.05	0.547	1.1504
4	FB_Low	0.541	0.3236	0.7	0.05	0.562	0.3736
Test #	Descript.	Initial height [mm]	Initial compaction [kg/m ^{3}]	Final Height [mm]	Final compaction [kg/m ^{3}]		
1	PC_High	165	167	55	500		
2	PC_Low	165	56	55	167		
3	FB_High	165	167	55	500		
4	FB_Low	165	56	55	167		

Table 4.3. Material sample parameters (PC-prepared cane; FB-final mill bagasse).

4.1.5 Error in experimental measurements

The sources of measurement error are shown in Table 4.4. The effects of these errors on secondary quantities such as material average compaction are determined by carrying the primary errors through the calculation process, and these are listed in Table 4.5. It is noted here that these errors are experimental only and do not involve the error sources associated with the image measurement procedure. These are to be addressed thoroughly within the results section of this chapter.

Primary error source	Error
Platen force	±0.1 kN
Platen position	±0.5 mm
Platen area	±0.00005 m ^{2}
Material mass	±1 g
Fibre content	±0.2 %

Table 4.4. Primary experimental errors.

Secondary quantity	Test	Nominal value	Range	Error [%]
Initial blanket height	all tests	165 mm	164 mm - 166 mm	±0.6
Final blanket height	all tests	55 mm	54 mm - 56 mm	±1.8
Initial sample compaction	PC_High	166.7	160.1 - 173.5	±4.0
[kg/m ^{3}]	PC_Low	55.6	53.4 - 57.8	±4.0
	FB_High	166.7	161.7 - 171.9	±3.1
	FB_Low	55.6	53.8 - 57.4	±3.2
Final sample compaction	PC_High	500	474.6 - 526.8	±5.3
[kg/m ^{3}]	PC_Low	166.7	158.3 - 175.5	±5.3
	FB_High	500	478.4 - 523.0	±4.6
	FB_Low	166.7	159.2 - 174.6	±4.7

Table 4.5. Approximate error in secondary experimental quantities.

Average sample compaction is the secondary quantity most affected by the sources of measurement error, with the maximum approximated error (±5%) resulting from the calculation of final sample compaction for the larger final mill bagasse experiment. It is noted here that local sample compactions may vary dramatically from the average sample values determined above, mostly due to the physical size of the experimental samples and the fibrous nature of the process materials.

4.1.6 Experimental results

Digital footage taken from each experiment was converted into a Quicktime© movie file and stored on the host computer. Each movie file was decomposed into a sequential series of images. The nature of the captured footage is displayed below in the form of initial and final images from two of the four experiments conducted. Platen load and displacement traces were captured over the duration of each experiment.

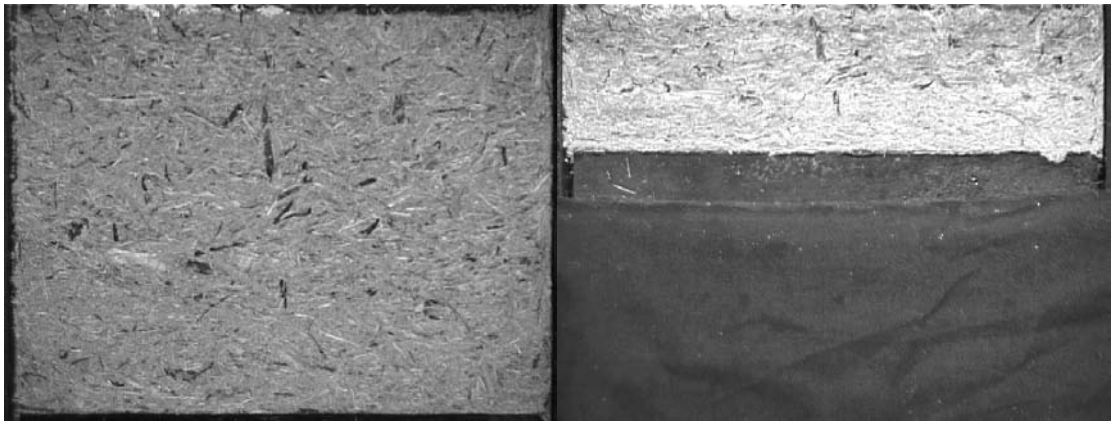

(a) Final bagasse high compaction.

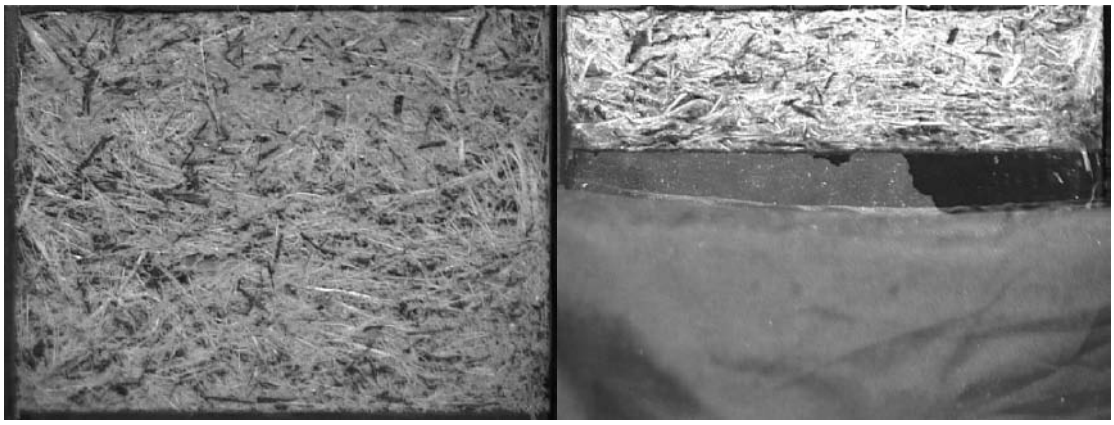

(b) Prepared cane low compaction

Figure 4.6. Image data.

Visual observation of the experiment footage indicates non–homogeneous behaviour within the samples, due to the discrete nature of prepared cane and bagasse and the large distribution of fibre size, and hence local stiffness. In the low compaction experiments material consolidation is low; hence material particles have more degrees of freedom, and large relative motions of individual particles were observed. This behaviour is notably more significant in the final bagasse low compaction experiment, in which material cohesion is low, due to the vacancy of sucrose–rich 'sticky' juice.

It is also evident from the video footage that the initial local density within each sample is not uniform, due also to the large distribution of fibre size resulting in a non-uniform void distribution. This phenomenon is enhanced in the upper regions of the high compaction samples, for which the MTS headstock was utilised to pre–compress the samples to the initial height of 165 mm. These problems associated with material inhomogeneity and initial sample conditions will be further addressed post–analysis.

4.1.6.1 Mechanical results

Figures 4.7 and 4.8 display the transient platen load traces for the low and high compaction experiments, respectively. For both ranges of compaction, the prepared cane experiment results in a higher applied load than the final bagasse experiment. This is due to the presence of larger constituent fibres and hence increased stiffness of prepared cane, as well as increased juice loadings associated with higher liquid content. Furthermore, material relaxation is more prominent for the prepared cane experiments due to dissipation of these higher juice pressures within the material sample.

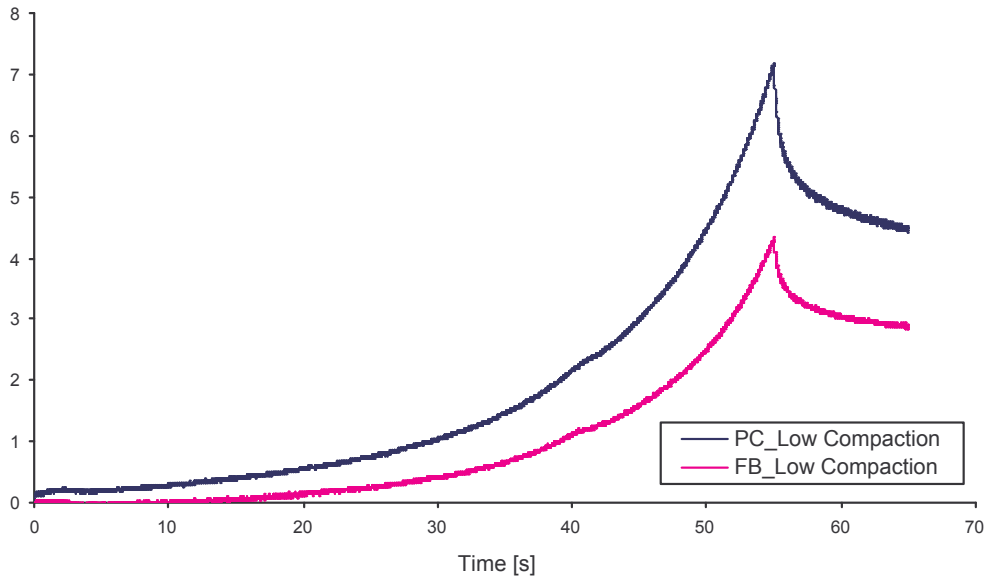

Figure 4.7. Platen load versus time plot for low compaction experiments.

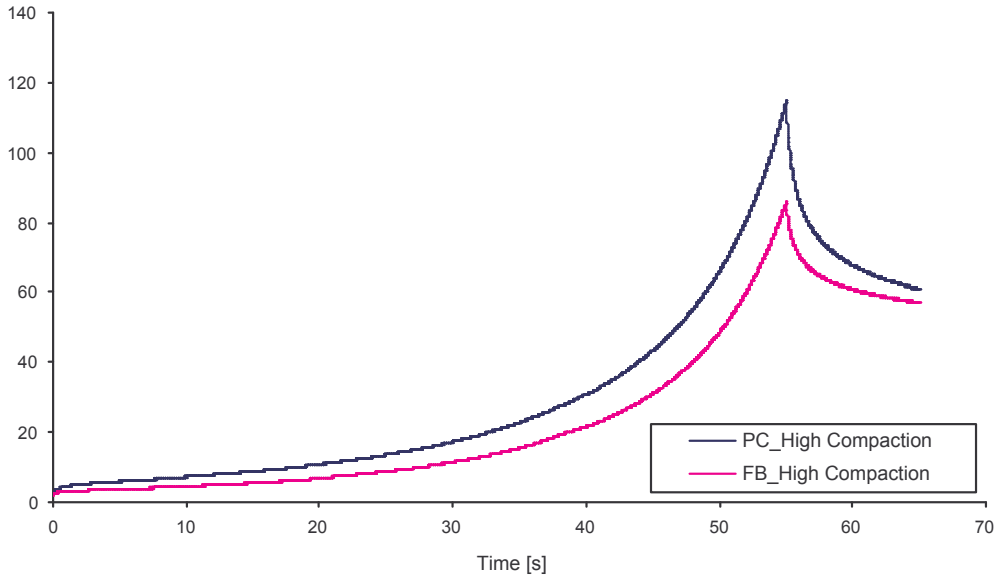

Figure 4.8. Platen load versus time plot for high compaction experiments.

4.1.6.2 Image measurement

In order to conduct ITA analyses on the images taken from the experiments, a range of numerical experiments were executed in order to determine the optimal numerical parameters for analysis of both materials.

4.1.6.3 Selection of sub-region size and time increment for image analysis

A factorial numerical experiment was conducted using the footage taken from the prepared cane and final bagasse low compaction experiments. The specific aim of this numerical analysis is to determine the optimal combination of time increment between images in the analysis and sub-region size for image analysis of the two materials. The low compaction scenario presents a worst case for each of the two materials, due primarily to the presence of larger air voids and less spatial restrictions for each particle within the assumed continuum.

In regard to selection of sub–region sizes for the experiment, it is noted (Westerweel 1993) that the bias error associated with the FFT correlation for a given sub–region size, is considered negligible at pixel–displacements less than one–quarter of the sub–region side length. Hence the ratio of the average sample pixel displacement and the sub-region size was utilised as an input variable for the experiment, rather than the sub-region size itself. This ratio incorporates the time

increment between images in each analysis, as the pixel displacement between two images is directly related to the time separation of the image pair.

Four sub-region sizes (8, 16, 32, 64) were tested against three pixel–displacement to sub-region size ratios ($1/16$, $1/8$, $1/4$) in order to determine the best combinations of parameters for image displacement measurement of prepared cane and bagasse. Assuming a linear displacement gradient vertically across the sample, the pixel–displacement in the centre of each sample was estimated as one half of the platen displacement, which is known to be travelling at 2 mm/s throughout each experiment. The values of time increment and sub-region size used in the numerical experiment are contained in Table 4.6.

Sub-region size	Sub-region size	Pixel-displacement to sub-region size ratio	Resulting image/time increment
[pixel x pixel]	[mm x mm]	[-]	[images/sec]
8 x 8	2.4 x 2.4	0.0625	4 / 0.16
		0.125	9 / 0.36
		0.25	18 / 0.72
16 x 16	4.8 x 4.8	0.0625	9 / 0.36
		0.125	18 / 0.72
		0.25	36 / 1.44
32 x 32	9.6 x 9.6	0.0625	18 / 0.72
		0.125	36 / 1.44
		0.25	72 / 2.88
64 x 64	19.2 x 19.2	0.0625	36 / 1.44
		0.125	72 / 2.88
		0.25	144 / 5.76

Table 4.6. Numerical experimental parameters.

A single point in the centre of each sample was chosen for assessment of the parameters. The correlation coefficient for the analysis point was stored for all available times in the transient analysis (see section 2.6 for correlation coefficient calculation method). Average correlation coefficient was thus determined as a measure of particle tracking confidence. The transient pixel position of the analysis point was followed manually through the image series to determine the actual final position of the analysis point for each experiment, to single pixel accuracy. Thus, the displacement error associated with the numerical particle–tracking algorithm was determined for each combination of the parameters. The results of the numerical experiment are contained in Tables 4.7 and 4.8 for the prepared cane low compaction

and final bagasse low compaction experiments, respectively. Negative values of percentage error correspond to the point displacing further than manually measured.

Sub-region size [pixel x pixel]	Pixel-displacement to sub-region size ratio [-]	Final (Y) position [pixel]	Avg. correlation coefficient [-]	Percentage error in (Y) displacement [%]
8 x 8	0.0625	157.5	0.58	31.8
	0.125	94.7	0.57	3.7
	0.25	110.0	0.52	10.5
16 x 16	0.0625	91.9	0.64	2.4
	0.125	92.1	0.62	2.5
	0.25	91.1	0.59	2.1
32 x 32	0.0625	95.8	0.74	4.1
	0.125	89.0	0.72	1.1
	0.25	86.4	0.64	0.0
64 x 64	0.0625	89.9	0.79	1.5
	0.125	86.9	0.73	0.2
	0.25	136.2	0.63	18.0

Table 4.7. Average correlation coefficient and percentage error in displacement results for the prepared cane low compaction experiment.

Sub-region size [pixel x pixel]	Pixel-displacement to sub-region size ratio [-]	Final (Y) position [pixel]	Avg. correlation coefficient [-]	Percentage error in (Y) displacement [%]
8 x 8	0.0625	162.02	0.6336	36.93
	0.125	101.92	0.6037	7.54
	0.25	107.87	0.5417	10.45
16 x 16	0.0625	102.89	0.6802	8.02
	0.125	104.48	0.6435	8.79
	0.25	101.14	0.5601	7.16
32 x 32	0.0625	98.69	0.7374	5.96
	0.125	87.18	0.7258	0.33
	0.25	86.97	0.6806	0.23
64 x 64	0.0625	84.45	0.8409	-1.00
	0.125	84.10	0.811	-1.17
	0.25	89.99	0.7435	-2.04

Table 4.8. Average correlation coefficient and percentage error in displacement results for the final bagasse low compaction experiment.

Figures 4.9 and 4.10 display the results contained in the above tables.

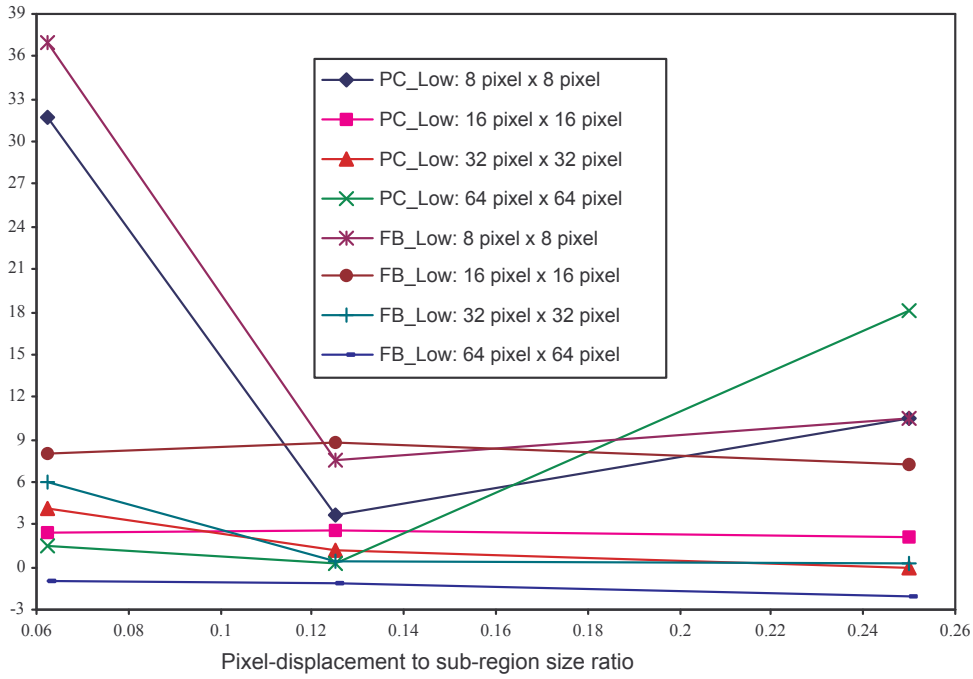

Figure 4.9. Graph showing the percentage error in (Y) displacement versus the pixel–displacement to sub–region size ratio at different sub–region sizes for prepared cane and final bagasse low compaction experiments.

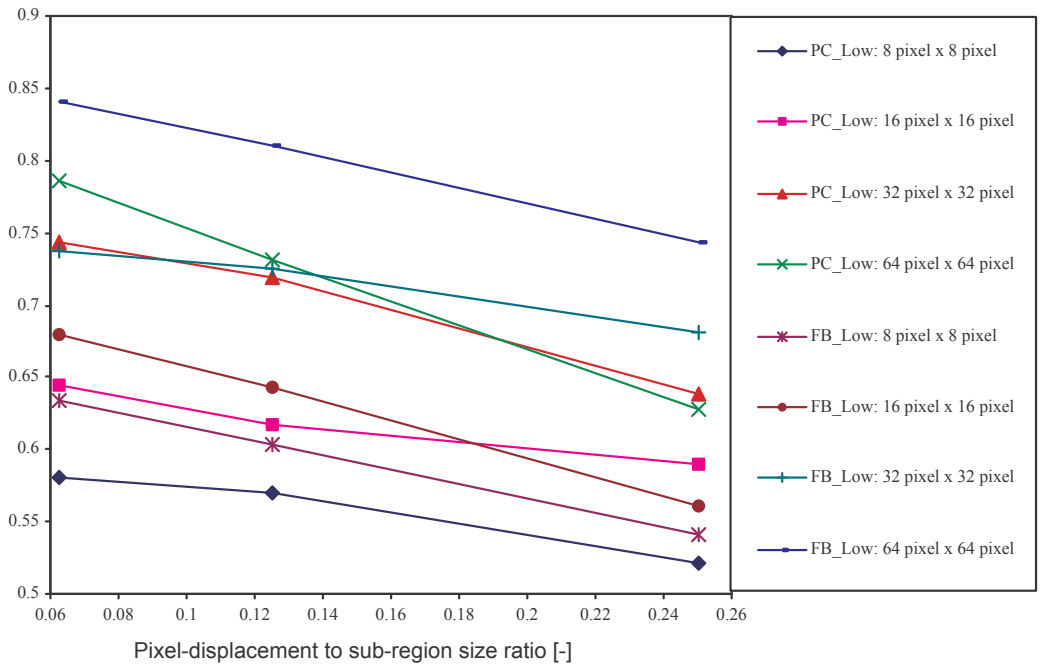

Figure 4.10. Graph showing the average correlation coefficient versus the pixel–displacement to sub–region size ratio at different sub–region sizes for prepared cane and final bagasse low compaction experiments.

Figure 4.9 shows that sub-region sizes less than 32 pixels produce quite erroneous results, especially at lower values of pixel–displacement to sub–region size ratios. The minimum error for both the low compaction experiments results from a 32 pixels sub–region and a displacement to size ratio of 0.25. Results for both materials show similar error trends for each sub–region size tested. The only significant exception is the 18 % error resulting from a 64 pixels sub–region and a displacement to size ratio of 0.25 for the prepared cane experiment. This large error is attributed to the inability of the particle–tracking algorithm to successfully deal with the onset of juice saturation, with such a large time increment (5.76 seconds) between images in the analysis. This is because juice saturation causes the local pixel pattern to change significantly over the large time step, and explains why the same trend was not observed in analysis of the final bagasse experiment, in which no juice saturation occurred.

Figure 4.10 shows that for a given sub–region size, the average correlation coefficient increases with decreasing displacement to size ratio. For a given value of pixel–displacement to sub–region size ratio, the average correlation coefficient is shown to increase with increasing sub–region size. Average correlation coefficient values are generally higher for the final bagasse experiment.

Having gained confidence in the ability of the particle tracking algorithm to successfully determine the final position of a point in the centre of a sample for each of the two materials, the following numerical investigation investigates the ability of the particle tracking algorithm to successfully determine the displacement of particles in the upper (low velocity) and lower (high velocity) regions of a given sample. This is an important investigation, as there is a considerable displacement gradient vertically across each sample. Hence, whilst a certain sub–region size/pixel–displacement to sub–region size ratio combination may accurately determine the final position of a particle in the blanket centre it may not succeed in tracking particles travelling at significantly different velocity. Considering displacement errors of less than 2 % to be accurate, Table 4.9 contains the combinations of sub–region size and pixel–displacement to sub–region size ratios that meet this 2 % error criterion.

In each of the low compaction experiments, a point was selected in both the upper and lower sections of the material sample for analysis with each combination of sub–region size and pixel–displacement to sub–region size ratio contained in Table 4.9. Average correlation coefficient and percentage error in displacement were again

determined as measures of particle tracking confidence and success. The results of this investigation are contained in Table 4.10 and Figures 4.11 and 4.12.

Test	Sub-region Size	Pixel-displacement to sub-region size ratio	Percentage error in (Y) displacement
[-]	[pixel x pixel]	[-]	[%]
PC_Low Compaction	32 x 32	0.125	1.1
		0.25	0.0
	64 x 64	0.0625	1.5
		0.125	0.2
FB_Low Compaction	32 x 32	0.125	0.3
		0.25	0.2
	64 x 64	0.0625	-1.0
		0.125	-1.2

Table 4.9. Suitable combinations of particle-tracking parameters for analysis of particle–tracking accuracy in the upper and lower regions of each material sample.

Test	Sample region	Sub-region size	Pixel-displ. to sub size ratio	Average correl. coefficient	Percent error in (Y) displacement
[-]	[-]	[pixel x pixel]	[-]	[-]	[%]
PC_Low	Lower	32 x 32	0.125	0.64	0.3
			0.25	0.53	91.7
		64 x 64	0.0625	0.74	-0.9
			0.125	0.71	-2.7
	Upper	32 x 32	0.125	0.77	0.9
			0.25	0.73	-2.3
		64 x 64	0.0625	0.83	-1.0
			0.125	0.80	-3.5
FB_Low	Lower	32 x 32	0.125	0.65	3.5
			0.25	0.07	108.9
		64 x 64	0.0625	0.81	1.2
			0.125	0.78	-0.1
	Upper	32 x 32	0.125	0.76	1.4
			0.25	0.74	0.7
		64 x 64	0.0625	0.82	0.5
			0.125	0.79	2.3

Table 4.10. Average correlation coefficient and percentage error in displacement results for the lower and upper regions of the low compaction samples.

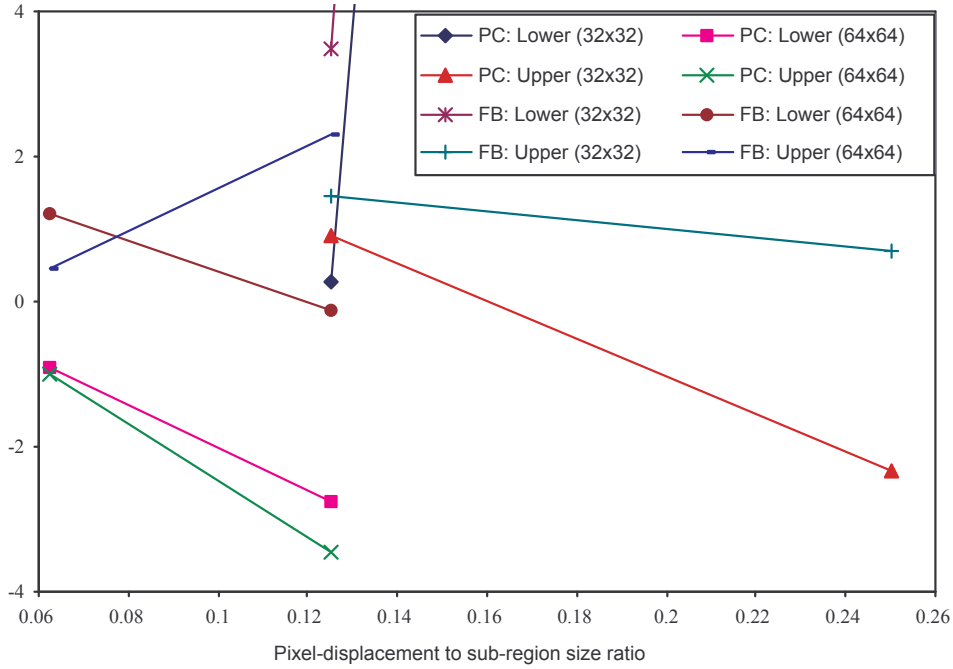

Figure 4.11. Graph showing the percentage error in (Y) displacement versus the pixel–displacement to sub–region size ratio in the upper and lower regions of the prepared cane and final bagasse low compaction experiments.

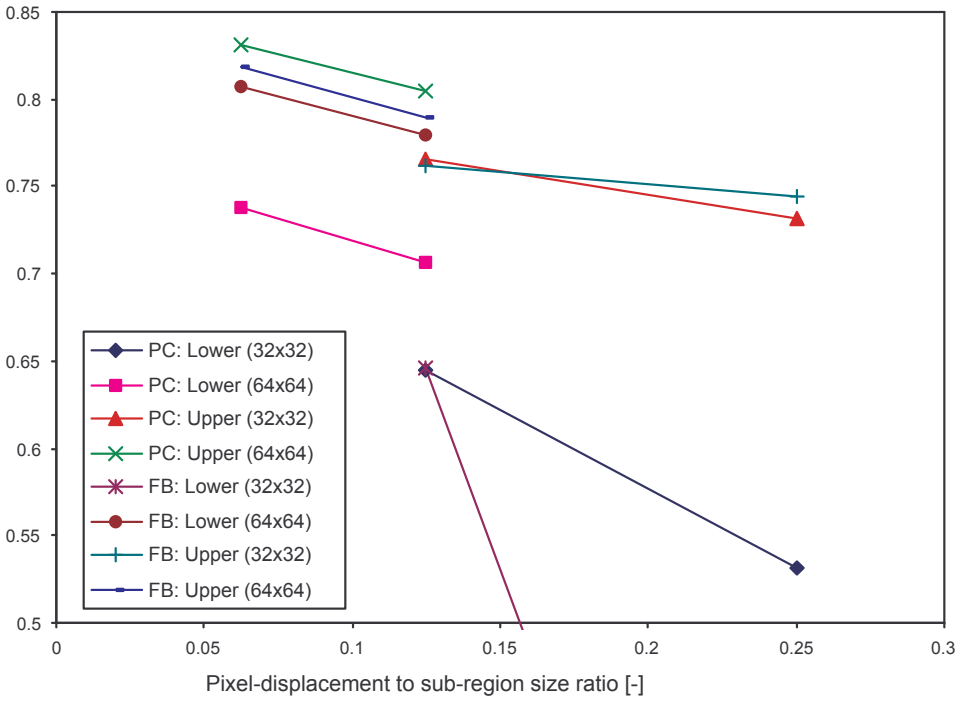

Figure 4.12. Graph showing the average correlation coefficient versus the pixel–displacement to sub–region size ratio in the upper and lower regions of the prepared cane and final bagasse low compaction experiments.

It is noted that in the upper region of a given sample, the total displacement during compression is low, hence increasing the percentage error in displacement with respect to that of a point in the centre of the sample. Likewise the lower section of a sample experiences large total displacement and errors are thus decreased with respect to that of a point in the centre of the sample. This displacement gradient across the sample depth is due to the testing procedure, in which the top platen remains stationary and the lower platen applies the constant 2mm/s compression.

Figure 4.11 shows that minimum error for both the upper and lower regions of the prepared cane low compaction experiment results from a 32 pixels sub-region and a pixel–displacement to sub–region size ratio of 0.125 (corresponding to an image increment of 36 images). Analysis of the final bagasse low compaction data shows that minimum error occurs at combinations of 64 pixels/0.0625 and 64 pixels/0.125 for the upper and lower regions, respectively.

Figure 4.12 indicates similar trends to the blanket centre results, with the average of the correlation coefficient increasing with increasing sub–region size and decreasing pixel–displacement to sub–region size ratio. The average correlation coefficient is also shown to increase with decreasing material velocity, resulting in higher correlation coefficient values for the upper regions of both samples.

In regard to ITA analysis of the full blanket, the data in Figure 4.11 indicates that, excluding the parameter combination 32 pixels/0.125, for which the particle–tracking algorithm fails to track the high velocity lower region of both samples, all tested combinations were considered acceptable for full blanket analysis, based on the 2% error criterion. The data in Figure 4.11 shows the optimal combination of sub–region size and pixel–displacement to sub–region size ratio, to be a sub–region size of 64 pixels and a displacement to sub–region size ratio of 0.0625 (corresponding to an image increment of 36 images). This combination of particle–tracking parameters is employed herein unless otherwise specified.

4.1.6.4 Selection of node spacing for image analysis

In order to achieve representative deformation results, the numerical ITA analysis grid must be appropriately sized in the direction of the compression, to avoid errors associated with excessive mesh distortion (Bear 1972). There are three limiting factors that must be considered when selecting the node spacing of the ITA grid. Firstly, as node spacing increases, so does the residual error associated with the finite

difference algorithm. However, for a fibrous material such as bagasse, there also exists a lower limit to node spacing, governed by the material preparation. That is, as the node spacing approaches the physical size of the larger fibres, errors will result from neighbouring nodes tracking together on a single bagasse fibre. Furthermore, the selection of sub–region size for analysis will influence the deformation results if sub–regions associated with neighbouring nodes are permitted to excessively overlap each other during material compression. Large sub–region overlaps will result in the particle–tracking algorithm measuring the same magnitude of displacement at neighbouring nodes, thus failing to correctly describe the displacement gradient across a sample. This phenomenon will affect the selection of node spacing for direct ITA analysis, but bears no significance for interpolation analyses, because the image displacement measurements are performed at fixed locations in a stationary grid.

A numerical experiment aimed at identifying suitable Y node spacing for direct ITA analysis for each experiment was conducted. ITA analyses involving various node spacings within a three–row by three-column grid were performed in order to determine an appropriate mesh density for full blanket analysis. The initial position of the grid centre point was kept constant with the grid expanding about this pixel location as node–spacing increased. Node spacings, ranging from 10 pixels (3 mm) to 140 pixels (42 mm) in 10 pixel increments, were tested for each of the four sighting trials. The effect of node spacing was examined by comparing the F22 component of the deformation gradient for each node–spacing analysed. The F22 component of the deformation gradient is the second order Taylor series approximation of the change in the y position of a grid node, with respect to its initial Y position in the reference or undeformed configuration. Hence, for confined uniaxial compression in the Y direction, F22 is the most significant component of the deformation gradient. For each of the four experiments, the final value of the F22 component of the deformation gradient at the centre node in the grid was plotted for all node spacings analysed. The results of this numerical analysis are shown in Figure 4.13.

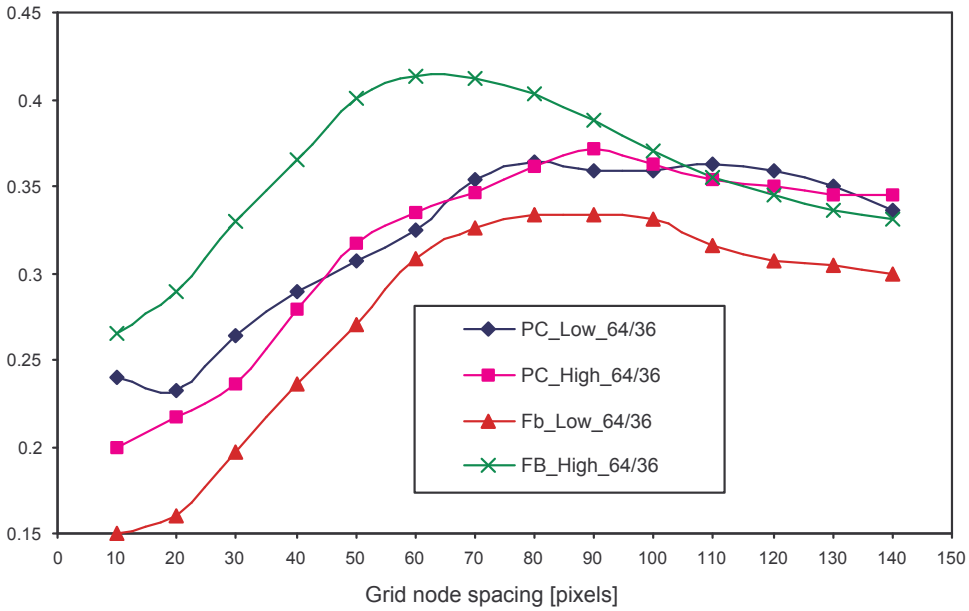

Figure 4.13. Graph showing the final value of the F22 component of the deformation gradient versus pixel node–spacing for all four sighting trials.

Results from the mesh density investigation show an underestimation of deformation at lower values of node spacing due to the combined influence of material particle size and sub–region overlap. Results for the prepared cane experiments experience this influence over a wider range of node spacing due to the presence of larger material particles. As node spacing increases, the predicted deformation climbs to a peak before dropping off due to the influence of error in the finite difference approximations employed to determine the component of the deformation gradient. Hence, for a given experiment, the range of node spacing over which the deformation plateaus is considered the ideal range for analysis.

4.1.6.5 ITA results

The combination of a 64 pixels sub–region and a time increment of 36 images (1.44 seconds) was selected along with suitable node spacing for ITA analysis of each of the four sighting trials. For each experiment, a uniform mesh covering the majority of the material sample was generated on the first image and tracked throughout the image series using the ITA direct measurement software. Table 4.11 contains the information required in the ITA parameters file for each of the four analyses.

Parameter	Definition	PC_LOW	FB_LOW	PC_HIGH	FB_HIGH
STX	X direction mesh start point [pixel#]	110	110	110	110
STY	Y direction mesh start point [pixel#]	4	8	14	6
KMAX	Number of nodes in the X direction [-]	13	13	13	13
IMAX	Number of nodes in the Y direction [-]	8	8	7	10
X1SHIFT	Node spacing in the X direction [pixels]	40	40	40	40
X2SHIFT	Node spacing in the Y direction [pixels]	80	80	91.83	62.11
OX1	Location of the origin in the X direction [pixel#]	390	390	390	390
OX2	Location of the origin in the Y direction [pixel#]	4	8	14	6
INPLAT	Initial Y pixel position of the bottom platen [pixel#]	564	563	565	565
TRAVEL	Platen pixel travel in the Y direction [pixels]	362	362	359	360
FIB	Fibre content of sample [-]	0.1861	0.5618	0.1695	0.5474
SMT	Total mass of sample [kg]	1.1277	0.3736	3.7145	1.1504
AP	Plan area of cell [m ^{2}]	0.0223	0.0223	0.0223	0.0223
HFEED	Initial blanket height [m]	0.165	0.165	0.165	0.165
RHOF	Density of fibre [kg/m ^{3}]	1530	1530	1530	1530
RHOJ	Density of juice [kg/m ^{3}]	1080	1080	1080	1080

Table 4.11. Parameters for preliminary ITA analysis.

The resulting deformed meshes for each of the four samples are shown below in Figures 4.14–4.17. The contoured variable shown in each figure is Y–Y Logarithmic strain.

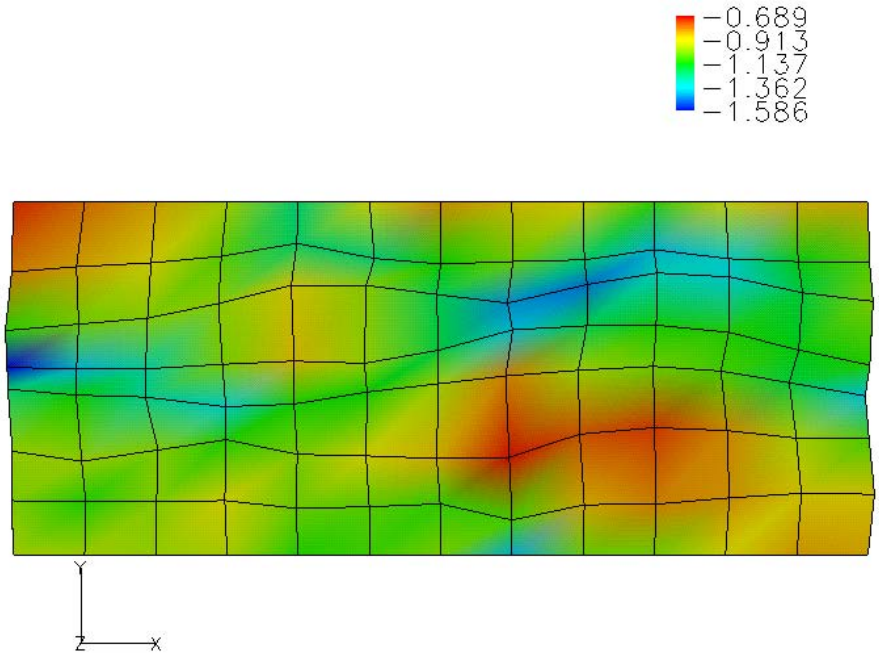

Figure 4.14. Prepared cane low compaction experiment: Y–Y Logarithmic strain.

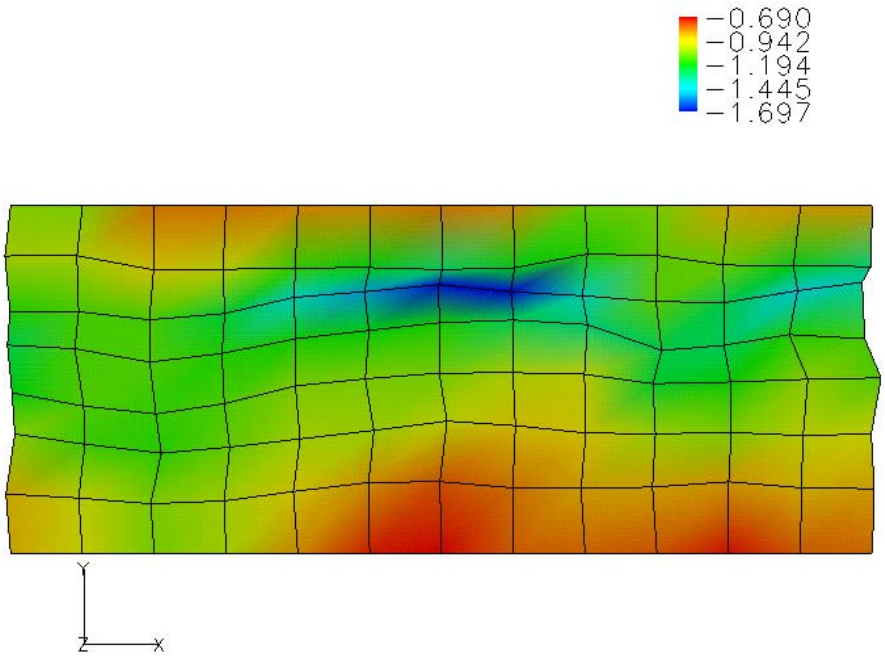

Figure 4.15. Final bagasse low compaction experiment: Y–Y Logarithmic strain.

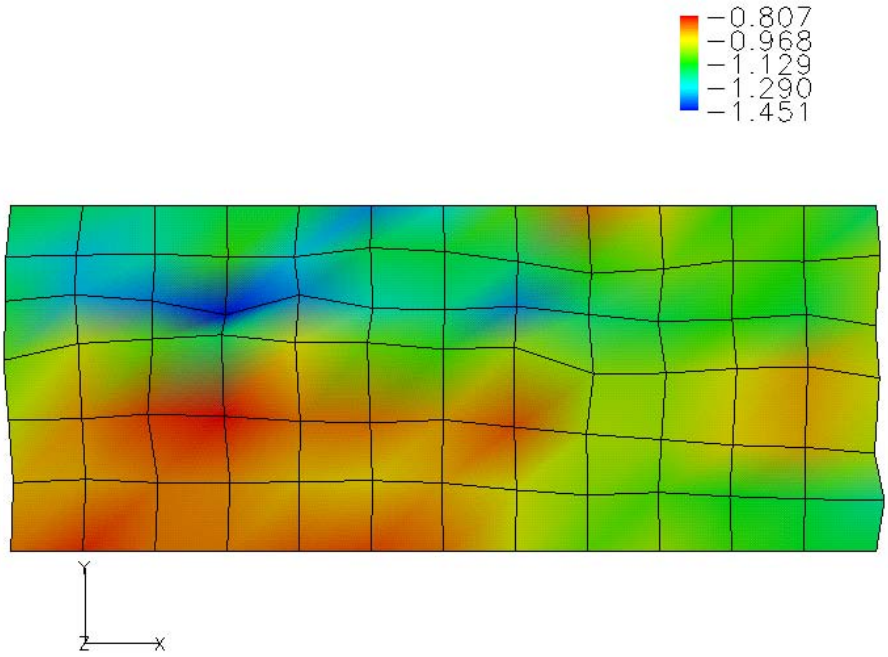

Figure 4.16. Prepared cane high compaction experiment: Y–Y Logarithmic strain.

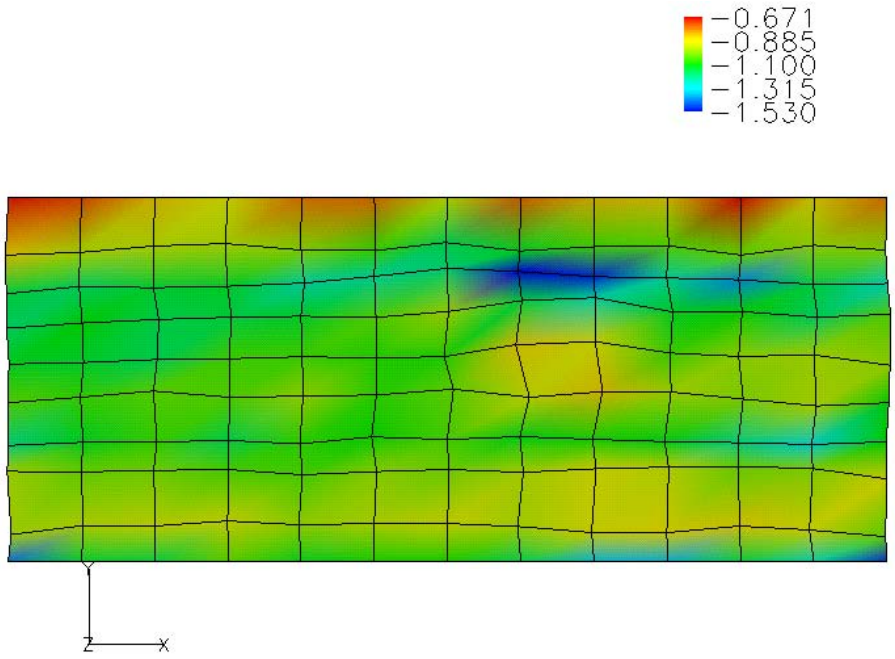

Figure 4.17. Final bagasse high compaction experiment: Y–Y Logarithmic strain.

The above figures show material inhomogeneity for the four analyses, in two distinctive forms:

1. Low deformation in the upper region of each material sample due to increased initial local stiffness. Manual observation and point tracking from the experimental image data confirms the accuracy of this result. This region of low deformation is due to loading the sample into the cell from the top and pre-compressing the sample to the initial height of 165 mm. Hence, as can be seen from the above figures, this region of low deformation is more substantial for the high compaction experiments, in which heavy pre-compression was required in order to reach the desired initial blanket height.
2. Large variations in material deformation within each sample due to discrete motion and random local stiffness within the blanket. Variations in local stiffness due to the large material fibre size distributions, results in discrete motion between different regions within the blanket. As the sample is deformed, stiff regions in the sample tend to force regions of lower stiffness to highly deform or to move away from the viewing plane into a region of high void. From the deformed meshes shown above, this

phenomenon is most prominent in the prepared cane low compaction experiment due to the larger fibre size distribution of the material and the presence of large regions of air voids. Large air voids provide spaces through the depth of the cell for material at the boundary to move into. Thus this result is an overestimation of true material strain and certainly indicates that the plane strain assumption of uniaxial compression is flawed for the depth of the cell and the range of material compaction tested in the experiments.

The magnitude and range of Y–Y Logarithmic strain experienced during compression is similar for all four analyses, with slightly higher local deformations experienced by the low compaction experiments, as might be expected. The final bagasse high compaction analysis shows the most uniform deformation during compression, due to higher initial consolidation and finer material preparation. There are also notable similarities in the deformed shapes for each of the two materials, irrespective of compaction range.

The ITA interpolation software (section 3.6.4) was employed in an effort to smooth the deformation results for each analysis, thus providing more suitable results for post–processing in regard to deformation trends. The resulting deformed meshes for each of the four samples are shown in Figures 4.18–4.21. Each mesh is again contoured with Y–Y Logarithmic strain.

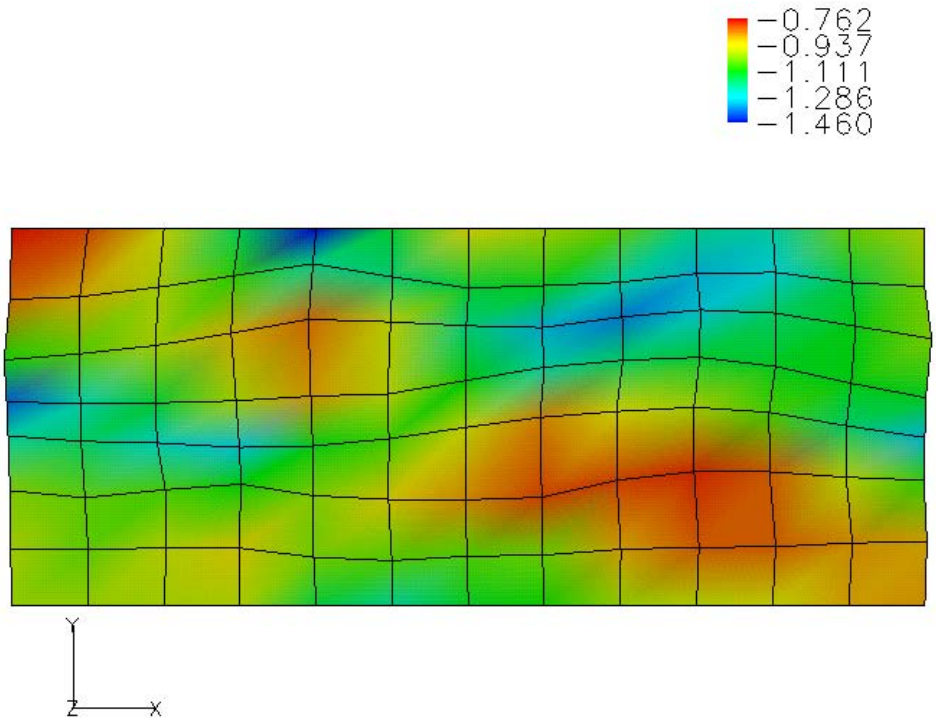

Figure 4.18. Prepared cane low compaction experiment: Y–Y Logarithmic strain, interpolated deformed mesh.

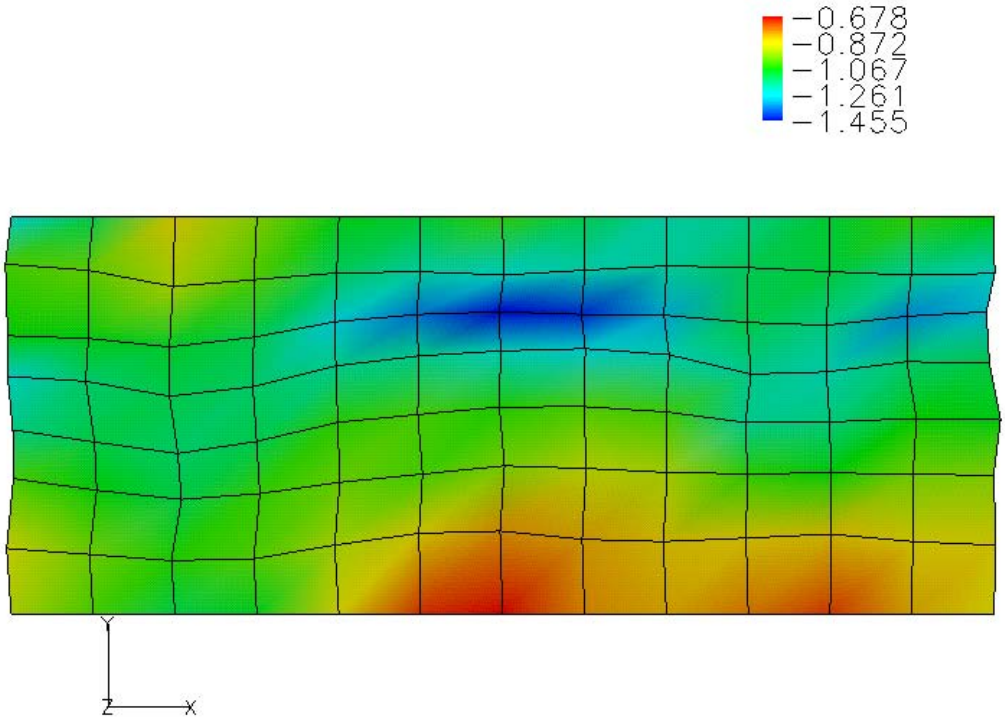

Figure 4.19. Final bagasse low compaction experiment: Y–Y Logarithmic strain, interpolated deformed mesh.

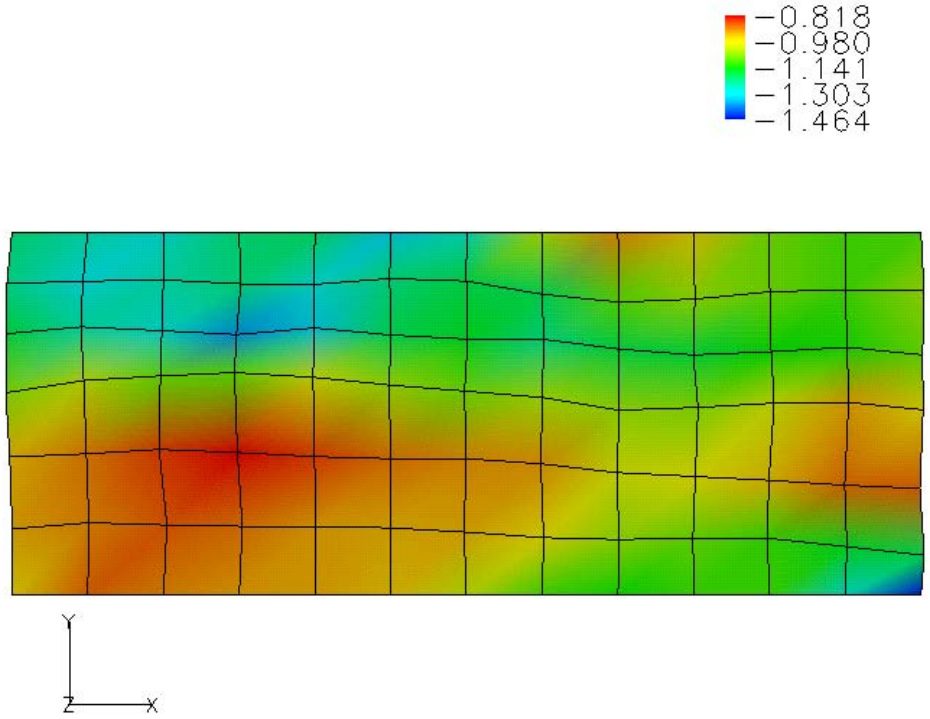

Figure 4.20. Prepared cane high compaction experiment: Y–Y Logarithmic strain, interpolated deformed mesh.

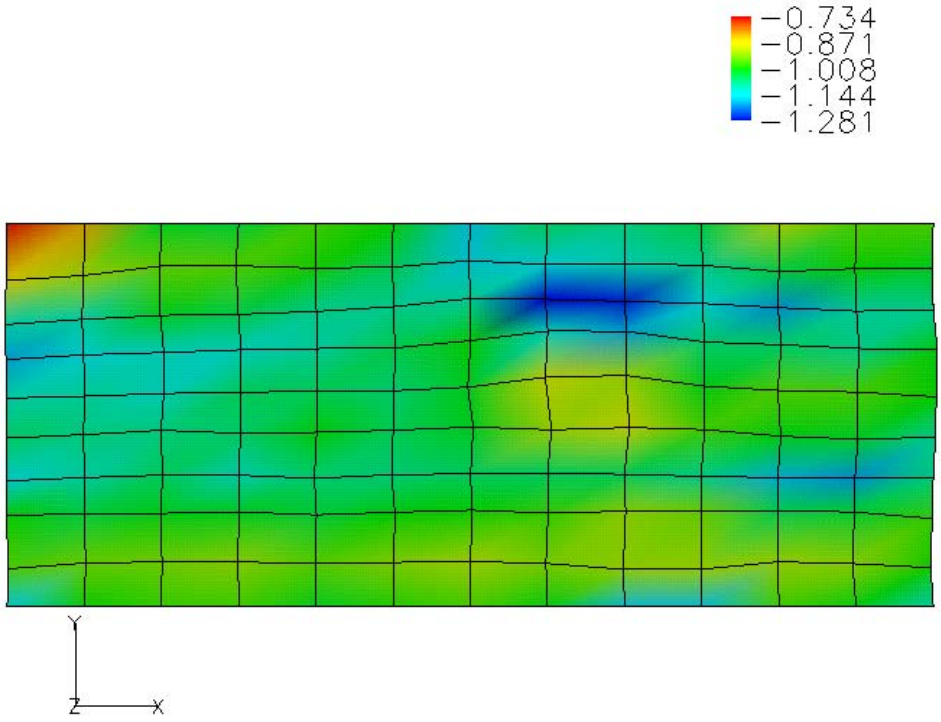

Figure 4.21. Final bagasse high compaction experiment: Y–Y Logarithmic strain, interpolated deformed mesh.

From the above contoured plots it can be seen that the ITA interpolation software smoothes the deformation results by reducing the range of the deformation results. In order to show the spread of data, the Y–Y Logarithmic strain results for the four interpolation analyses were plotted against the Y axis (blanket depth) as shown in Figure 4.22.

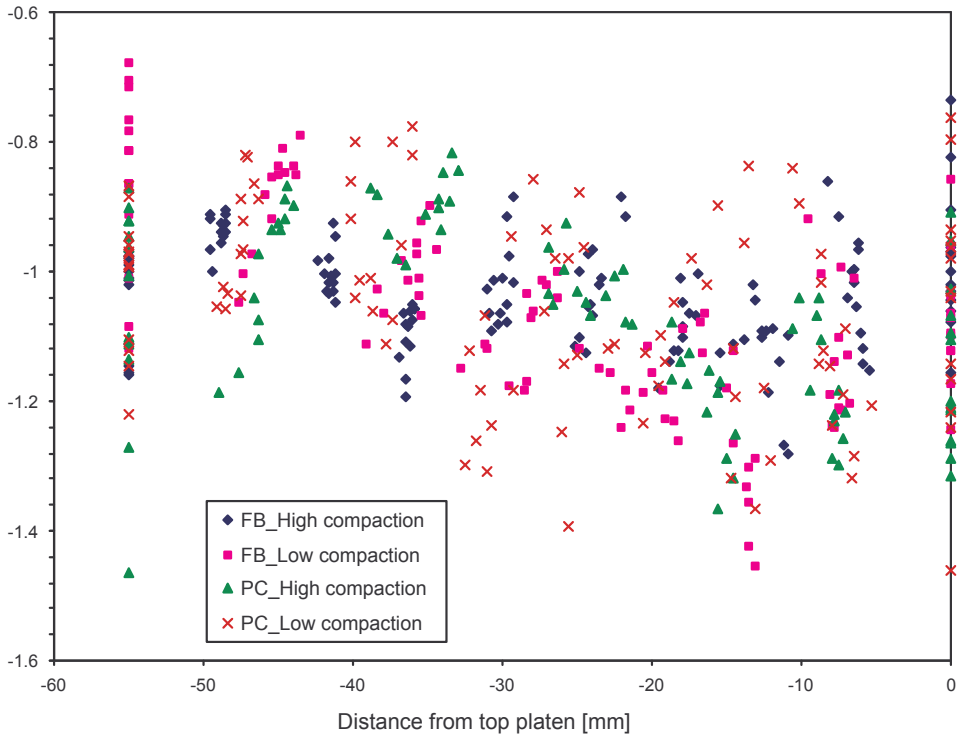

Figure 4.22. Graph showing the Y–Y Logarithmic strain data for all four sighting trial interpolation analyses.

From visual inspection and manual particle tracking, the ITA results accurately represent the true deformation experienced by the majority of each sample during compression. However, these results show strongly that both prepared cane and bagasse display non-homogenic behaviour in all of the four experiments conducted. In order to obtain useful deformation results, refinement of experimental practices is required. The most obvious alterations to the testing procedure are to load the sample perpendicular to the axis of compression, and to reduce the depth of the cell. Whilst this will significantly reduce the variation in local stiffness due to the loading technique and pre-compression, it does not address the evident inhomogeneity of the material due to the distribution of fibre size and hence stiffness. In order to achieve

material homogeneity, testing with sieved samples containing more uniformly sized fibres is required. Furthermore, analysis of the sighting trials identified the need for repeat experiments in order to determine the repeatability of deformation results. An auxiliary experiment was thus conducted in order to validate the above hypotheses.

4.2 The auxiliary trials

The auxiliary trials involved four final bagasse, four fines experiments and a one–off coarse fibre test. All of the nine experiments involved the same geometric compression and material mass, hence providing four repeat experiments for each primary material tested. Final bagasse was collected from the final mill on the A-side milling train at Invicta sugar-mill. The fines material was created by sieving the final bagasse in a three–sieve stack containing sieves with apertures of 11 mm, 7 mm and 2.5 mm. The material (or fines) that passed through the entire stack was collected in a tray and used for testing. It is noted that approximately sixty–five percent of the final bagasse sieved was fines.

4.2.1 Aims and scope of the experimental program

The aims of the experimental program are to:

1. Improve the material testing procedure.
2. Collect visual data for image measurement analysis.
3. Measure the 2D local fibre deformation field for each material sample.
4. Assess the repeatability of ITA results for both final bagasse and fines.

Experimental program scope:

1. All final bagasse experiments were conducted using material from the same sample of bagasse taken from Invicta mill.
2. All fines experiments were conducted using material sieved from the same sample of final bagasse taken from Invicta mill.
3. Time series of digital images were collected for all experiments.
4. Juice extraction was given no consideration.

4.2.2 Apparatus modifications

The depth of the uniaxial cell was reduced from 98 mm to 25 mm in order to restrict material motion in this direction (away from the viewing plane). This was achieved by using the existing cell with a 73 mm thick Perspex spacer that was also utilised for sample pre–compression perpendicular to sample compression. A new 25 mm thick top platen was also fabricated to comply with the reduced cell depth. A leather seal was employed on the viewing side of both platens.

4.2.3 Procedure

Final bagasse was collected from the last mill on the A-side milling train at Invicta mill and stored at -4°C. All bagasse tests were conducted using material from one container of collected bagasse. The bagasse was thoroughly mixed and two 500 gram samples were taken for fibre content analysis. The results of the fibre tests are shown below in Table 4.12.

Sample #	1	2
Initial bagasse mass [g]	500	500
Mass out 1 [g]	2620.3	2859.9
Mass out 2 [g]	2620.2	2859.8
Mass of hot dry can [g]	2356.8	2589.5
Fibre mass [g]	264.4	270.3
Fibre content	0.5288	0.5406
Average fibre content	0.5347	

Table 4.12. Invicta mill final mill bagasse fibre content analysis.

The fines material was created by sieving four kilograms of final bagasse in a stack containing three sieve sizes (11mm, 7mm, 2.5mm). The material that was fine enough to pass through the stack was collected in a tray and thoroughly mixed for testing. This was approximately sixty–five percent by mass of the final bagasse used. Two 200 gram samples were taken for fibre content determination. A stocking was utilised to prevent loss of the fines material during the fibre content analysis. The results of the fibre tests are shown below in Table 4.13. The material in the sieves

was remixed to form the coarse fibre material. The fibre content of the coarse material was not determined.

Sample #	1	2
Initial fines mass [g]	200	200
Mass out 1 [g]	114.4	113.4
Mass out 2 [g]	114.2	113.3
Mass of hot stocking [g]	4.0	4.0
Fibre mass [g]	110.2	109.3
Fibre content	0.551	0.5465
Average fibre content	0.549	

Table 4.13. Fines material fibre content analysis.

The testing cell was placed on its side, with the viewing window face down. A piece of 12 mm ply was placed across the cell at the sample initial height as a barrier for sample loading. This is shown below in Figure 4.23.

Figure 4.23. Perpendicular sample loading.

Material seed was distributed evenly over the viewing window prior to sample loading. This was considered a significant advantage over the previous method of premixing the seed with the sample, because a uniform distribution of the seed across the viewing plane was achieved. The material samples were loaded into the cell as evenly and freely as possible, such that local material consolidation was avoided. The Perspex spacer was utilised to pre–compress the sample against the glass (or perpendicular to the direction of compression) in order to minimise variations in

initial material properties in the direction of compression. The steel side–plate was then placed onto the upward side of the cell and bolted in place. The testing cell was then lifted into the upright position, the ply barrier was removed and the cell was placed onto the MTS ram. The top platen attached to the MTS headstock was then brought down to the top of the material sample (initial height of 170 mm) and the headstock was locked in place for testing. Each sample was then compressed at a constant velocity of 2 mm/s to a final height of 60 mm and held at the final height for 15 seconds. Load and displacement data were recorded and stored in data files corresponding to each experiment.

4.2.4 Experimental program

The experimental program aimed to obtain repeatable deformation mappings for the two primary materials and also to show the strain field for the larger or coarse fibres. The mass and geometric configuration was thus kept constant for all tests. The sample mass was chosen to give a compaction range in the vicinity of 100–300 kg/m^3 for all tests. The experimental program is shown below in Table 4.14.

Test #	Material	Mass	Initial height	Initial compaction	Final height	Final compaction
[-]	[-]	[kg]	[mm]	[kg/m ^{3}]	[mm]	[kg/m ^{3}]
1	FB	0.1765	169	98	59	281
2 (RPT)	FB	0.1765	169	98	59	281
3 (RPT)	FB	0.1765	169	98	59	281
4 (RPT)	FB	0.1765	169	98	59	281
5	FINES	0.1765	169	101	59	289
6 (RPT)	FINES	0.1765	169	101	59	289
7 (RPT)	FINES	0.1765	169	101	59	289
8 (RPT)	FINES	0.1765	169	101	59	289
9	COARSE	0.1765	169	97	59	278

Table 4.14. Auxiliary trials program.

4.2.5 Error in experimental measurements

The sources of measurement error are as per the sighting trials. The effects of these errors on secondary quantities such as material average compaction are listed in Table 4.15.

Secondary quantity	Test	Nominal value	Range	Error [%]
Initial blanket height [mm]	all tests	169	168 - 170	±0.6
Final blanket height [mm]	all tests	59	58 - 60	±1.7
Initial sample compaction	FB	98	96.4 - 99.6	±1.63
[kg/m ^{3}]	FINES	100.8	99.3 - 102.3	±1.5
Final sample compaction	FB	280.8	273.5 - 288.3	±2.7
[kg/m ^{3}]	FINES	288.7	281.0 - 296.4	±2.7

Table 4.15. Error in secondary experimental quantities.

Average sample compaction is again the secondary quantity most affected by the primary sources of error, with the maximum approximated error (±2.7%) resulting from the calculation of final sample compaction for all experiments.

4.2.6 Image measurement results

Video footage taken from each experiment was converted into a Quicktime© movie file and stored on the host computer. Each movie file was decomposed into a sequential series of images. The nature of the captured footage is displayed in Figure 4.24, in the form of initial and final images from two of the experiments conducted.

Figure 4.24. Image data: a) Final bagasse.

Figure 4.24. Image data: b) Fines.

Visual observation of the experiment footage indicates a significant improvement in initial material homogeneity due to the perpendicular sample pre–compression. Furthermore, material motions away from the viewing plane during compression are basically eliminated, resulting in pixel pattern integrity throughout each experiment. Frictional effects are evident in the regions of material near the vertical cell boundaries.

The combination of a sub–region size of 64 pixels and a displacement to sub–region size ratio of 0.0625 (corresponding to an image increment of 36 images or 1.44 seconds) was selected for ITA direct analysis of the nine experiments (Section 4.1.6.3). Suitable node spacings in the vicinity of 100 pixels were chosen in order to eliminate the effects of sub–region overlap and maximum particle size on the deformation results. For each experiment, a uniform mesh covering the majority of the material sample was generated on the first image and tracked throughout the image series using the ITA direct measurement software. The regions of the sample close to the vertical cell boundaries were excluded due to the frictional influence on the deformation in these regions.

4.2.6.1 Final bagasse

Table 4.16 contains the information required in the ITA parameters file for the four final bagasse tests.

Parameter	Definition	FB_01	FB_02	FB_03	FB_04
STX	X direction mesh start point [pixel#]	110	110	110	110
STY	Y direction mesh start point [pixel#]	30	19	23	29
KMAX	Number of nodes in the X direction [-]	13	13	13	13
IMAX	Number of nodes in the Y direction [-]	6	6	6	6
X1SHIFT	Node spacing in the X direction [pixels]	40	40	40	40
X2SHIFT	Node spacing in the Y direction [pixels]	103.8	103.8	103.6	101.6
OX1	Location of the origin in the X direction [pixel#]	390	390	390	390
OX2	Location of the origin in the Y direction [pixel#]	30	19	23	29
INPLAT	Initial Y pixel position of the bottom platen [pixel#]	549	538	541	537
TRAVEL	Platen pixel travel in the Y direction [pixels]	328	325	327	322
FIB	Fibre content of sample [-]	0.535	0.535	0.535	0.535
SMT	Total mass of sample [kg]	0.1765	0.1765	0.1765	0.1765
AP	Plan area of cell [m ^{2}]	0.0057	0.0057	0.0057	0.0057
HFEED	Initial blanket height [m]	0.169	0.169	0.169	0.169
RHOF	Density of fibre [kg/m ^{3}]	1530	1530	1530	1530
RHOJ	Density of juice [kg/m ^{3}]	1080	1080	1080	1080

Table 4.16. Parameters for ITA analysis of the final bagasse tests.

The resulting deformed mesh for each of the four final bagasse experiments are shown in Figures 4.25–4.28. The contoured variable shown in each figure is Y–Y Logarithmic strain.

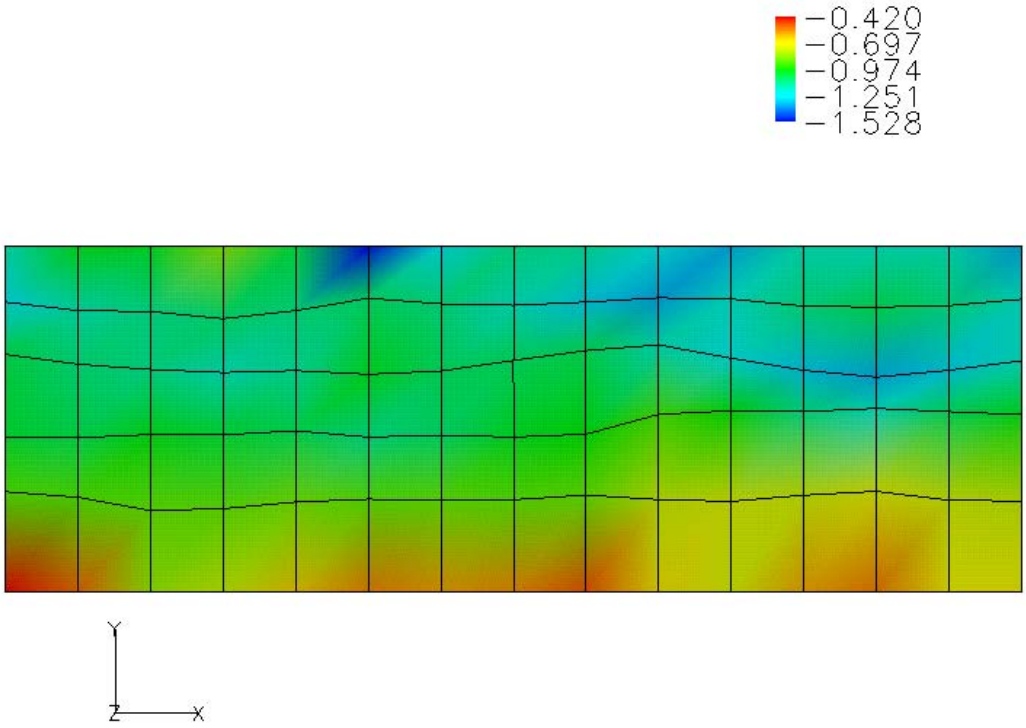

Figure 4.25. Deformed mesh: Final bagasse Test 01, Y-Y Logarithmic Strain.

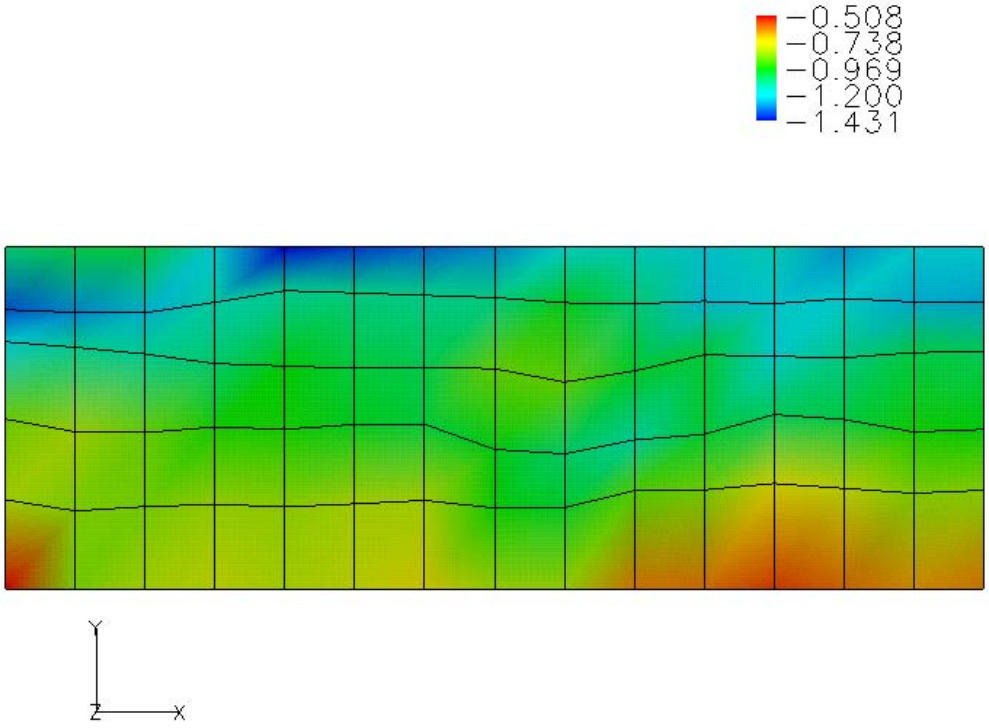

Figure 4.26. Deformed mesh: Final bagasse Test 02, Y-Y Logarithmic Strain.

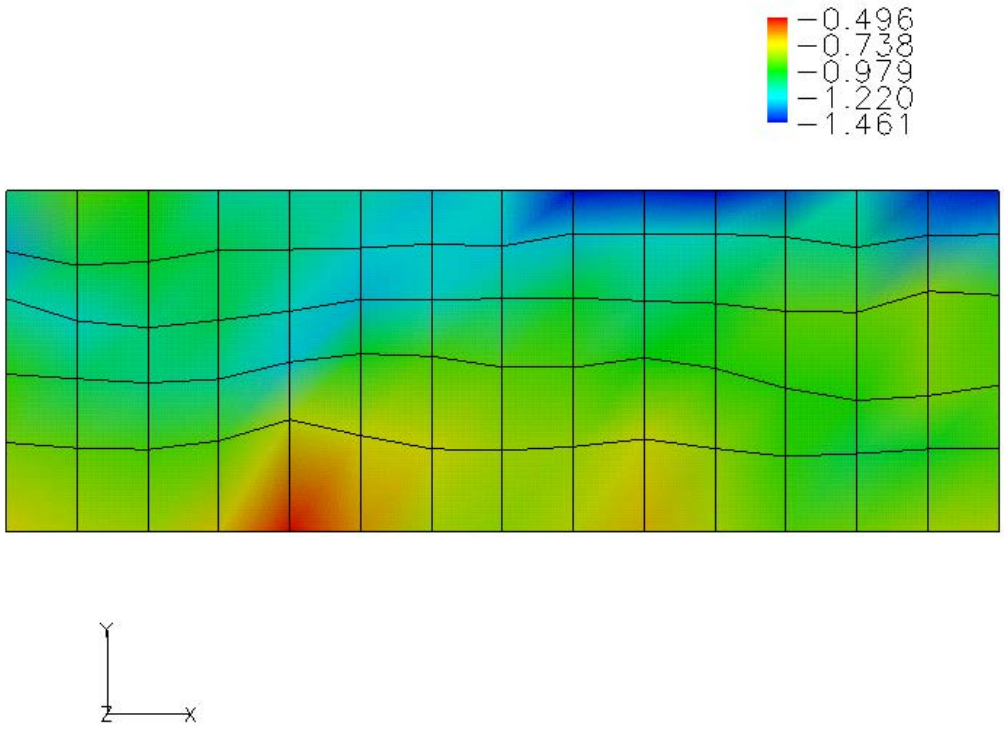

Figure 4.27. Deformed mesh: Final bagasse Test 03, Y-Y Logarithmic Strain.

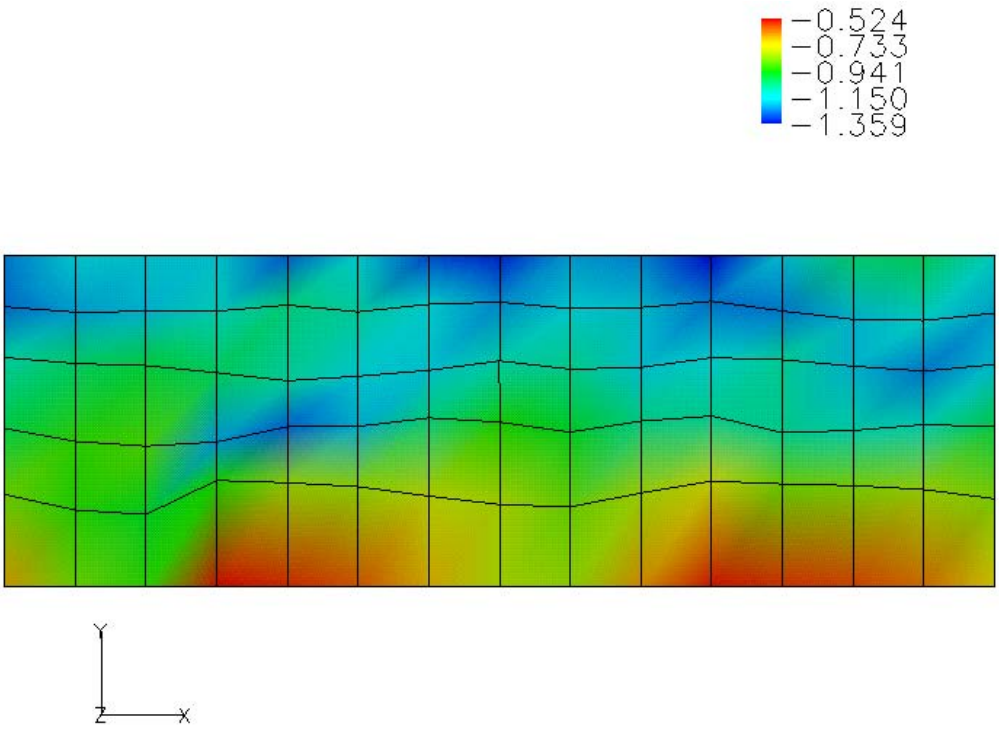

Figure 4.28. Deformed mesh: Final bagasse Test 04, Y-Y Logarithmic Strain.

The results show repeatable deformations and indicate a definite trend in deformation across the depth of all four samples. As would be expected due to cell wall friction, the highest deformation is in the material near the top or moving platen. There is also a strong gradient in deformation across the sample, resulting in low deformation in the region of the bottom or fixed platen. Hence, decreasing the cell depth and employing perpendicular sample loading has significantly reduced the variation in initial material density, resulting in repeatable deformation trends across the material samples. The Y–Y Logarithmic strain data shown in the above figures were plotted for all four final bagasse tests, and linear approximations to each of the four data series were applied in order to assess the validity of linear deformation across the sample depth and also the repeatability of the deformation results.

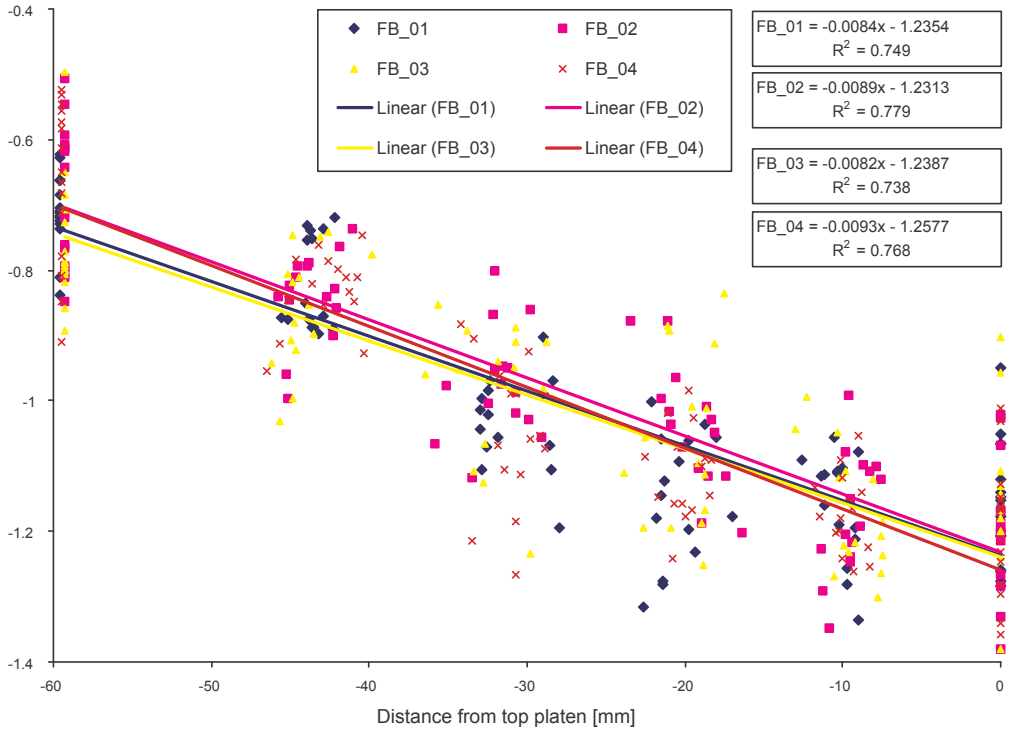

Figure 4.29. Graph showing the Y–Y Logarithmic strain versus sample depth for the four final bagasse tests.

Figure 4.29 shows stronger repetition in the auxiliary trials final bagasse deformation results than for the sighting trials. The applied linear approximations for the four data series are of similar statistical significance and present an acceptable representation of the Y–Y Logarithmic strain data. However, there is significant variance in the Y–Y Logarithmic strain data for a given horizontal slice of each sample. Such variance is at this stage assumed to be due to the large fibre size distribution of final bagasse.

The ITA interpolation software was applied to the final bagasse tests to smooth the deformation data. Results showed only a slight reduction in the spread of the data, as can be seen for the first final bagasse test (FB_01) in Figure 4.30.

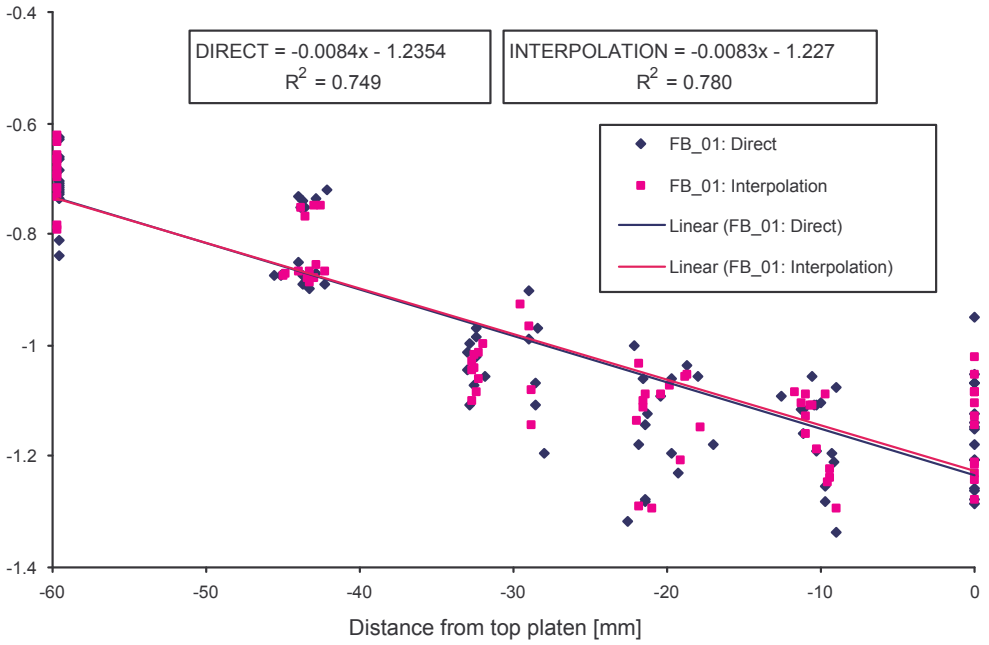

Figure 4.30. Comparison of direct and interpolated results for the first final bagasse test (FB_01).

4.2.6.2 Fines

Table 4.17 contains the information required in the ITA parameters file for the four fines tests. The deformed meshes for each of the four samples are shown in Figures 4.31–4.34. The contoured variable shown in each figure is the Y–Y Logarithmic strain.

Parameter	Definition	FINES_01	FINES_02	FINES_03	FINES_04
STX	X direction mesh start point [pixel#]	110	110	110	110
STY	Y direction mesh start point [pixel#]	22	24	30	26
KMAX	Number of nodes in the X direction [-]	13	13	13	13
IMAX	Number of nodes in the Y direction [-]	6	6	6	6
X1SHIFT	Node spacing in the X direction [pixels]	40	40	40	40
X2SHIFT	Node spacing in the Y direction [pixels]	104	103.6	103.8	104.2
OX1	Location of the origin in the X direction [pixel#]	390	390	390	390
OX2	Location of the origin in the Y direction [pixel#]	22	24	30	26
INPLAT	Initial Y pixel position of the bottom platen [pixel#]	542	541	551	547
TRAVEL	Platen pixel travel in the Y direction [pixels]	327	325	327	330
FIB	Fibre content of sample [-]	0.55	0.55	0.55	0.55
SMT	Total mass of sample [kg]	0.1765	0.1765	0.1765	0.1765
AP	Plan area of cell [m^2]	0.0057	0.0057	0.0057	0.0057
HFEED	Initial blanket height [m]	0.169	0.169	0.169	0.169
RHOF	Density of fibre [kg/m^3]	1530	1530	1530	1530
RHOJ	Density of juice [kg/m^3]	1080	1080	1080	1080

Table 4.17. Parameters for ITA analysis of the fines tests.

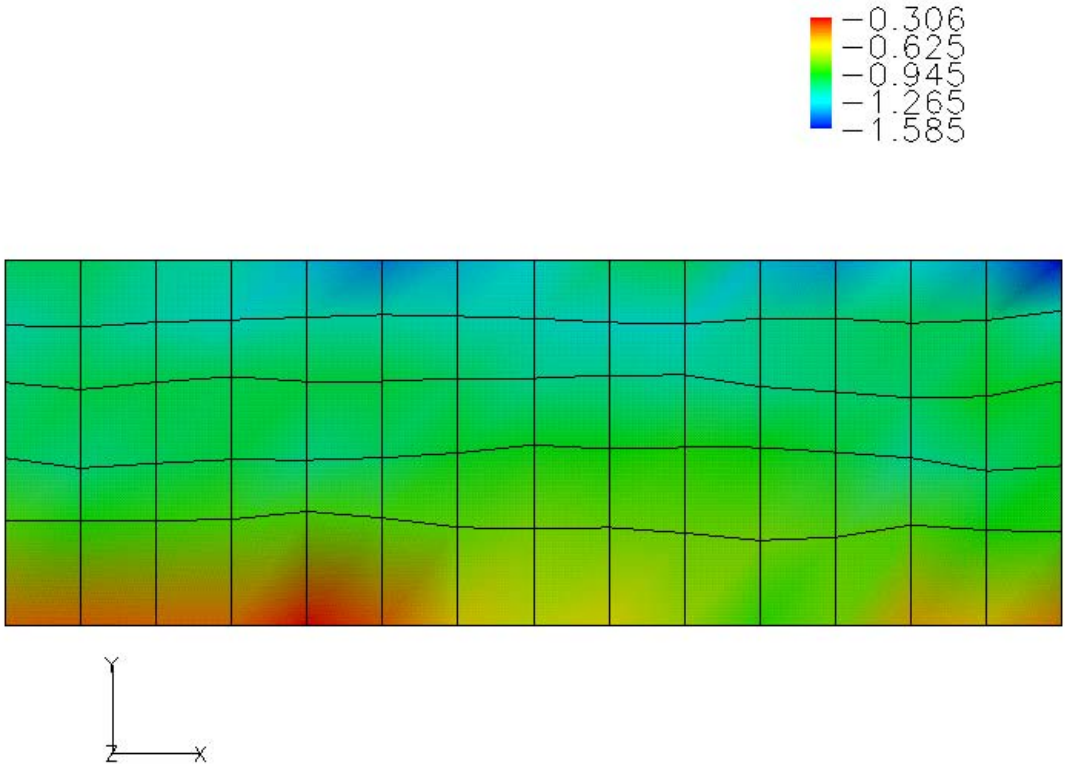

Figure 4.31. Deformed mesh: Fines Test 01, Y-Y Logarithmic Strain.

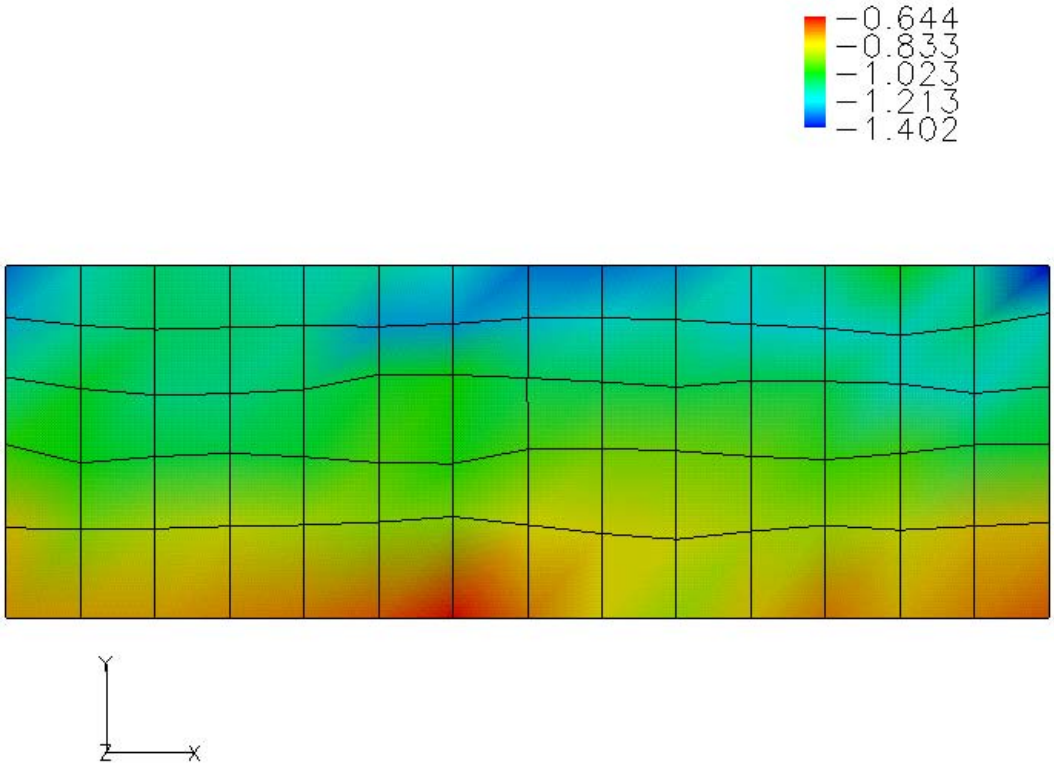

Figure 4.32. Deformed mesh: Fines Test 02, Y-Y Logarithmic Strain.

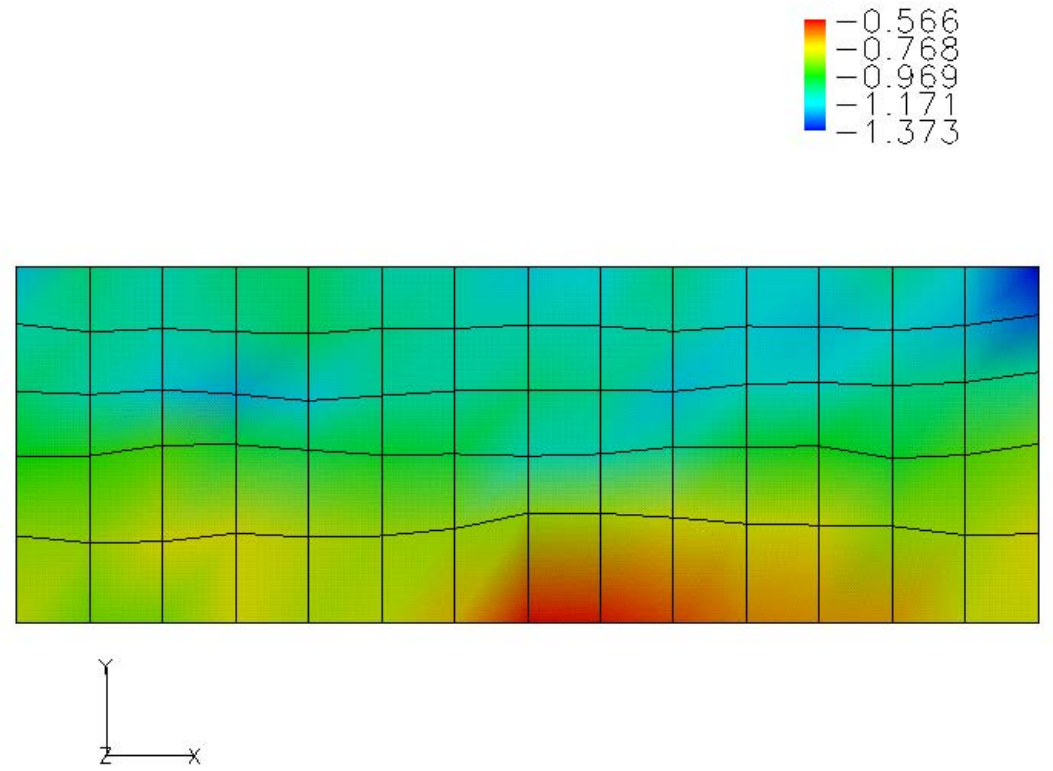

Figure 4.33. Deformed mesh: Fines Test 03, Y-Y Logarithmic Strain.

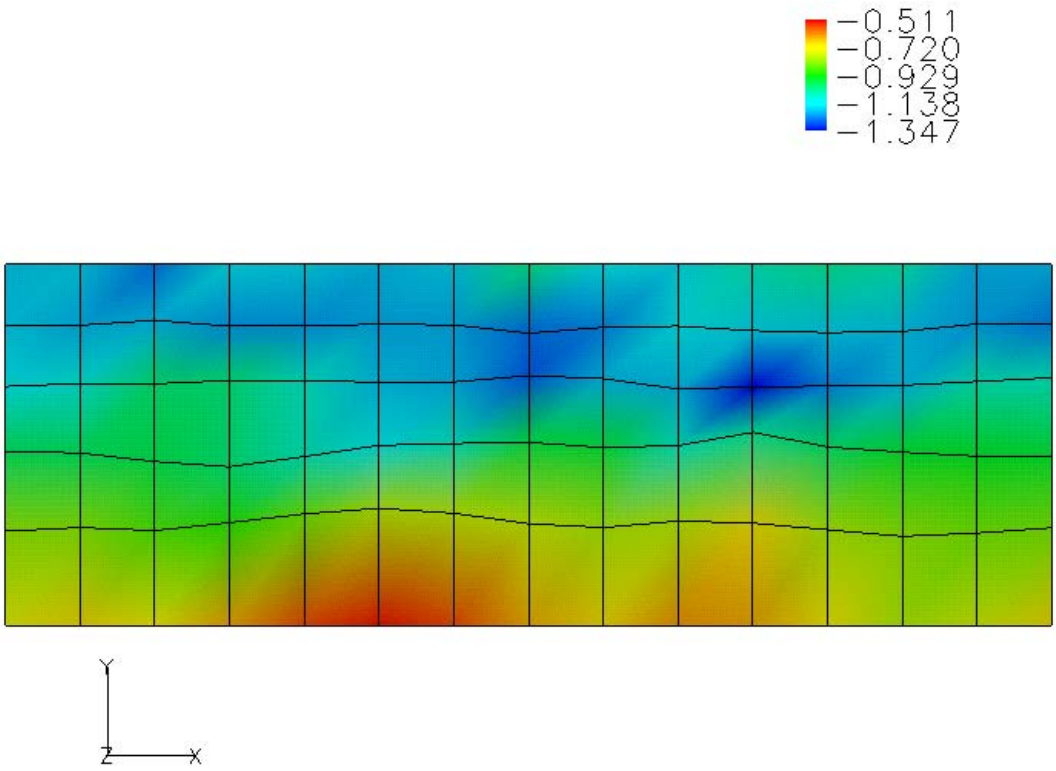

Figure 4.34. Deformed mesh: Fines Test 04, Y-Y Logarithmic Strain.

The ITA deformed mappings of the four fines samples show the same frictional trend in deformation across the sample depth that was observed in the final bagasse tests, with the magnitude of deformation decreasing with distance from the top or moving platen. The Y–Y Logarithmic strain results were plotted for all four fines tests and linear approximations were applied to each of the four data series in order to assess the validity of assuming a linear deformation across the sample depth and also the repeatability of the deformation results.

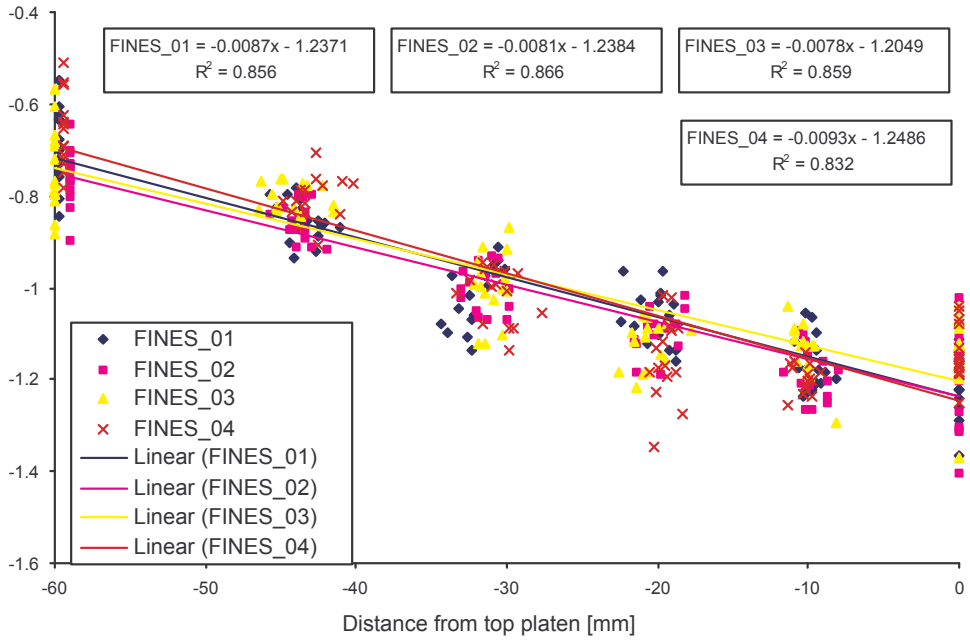

Figure 4.35. Graph showing the Y–Y Logarithmic strain versus sample depth for the four fines tests.

Figure 4.35 indicates that the deformation of the fines samples is significantly smoother than that of final bagasse, as can be seen from the improved statistical significance of the linear approximations applied to the strain data. Hence, the hypothesis that the large variance in deformation data for the final bagasse tests is due to the increased fibre size distribution has been validated.

4.2.6.3 Coarse Fibre

The single coarse fibre test was analysed using the ITA direct software. The deformed mesh is contoured with the Y–Y Logarithmic strain and shown in Figure 4.36. The strain results are also graphed in Figure 4.37. The deformation of the coarse fibres is certainly erratic, with large variations in strain within a given horizontal slice of the blanket. The linear approximation is of low statistical significance as a result of this large variance in the strain data.

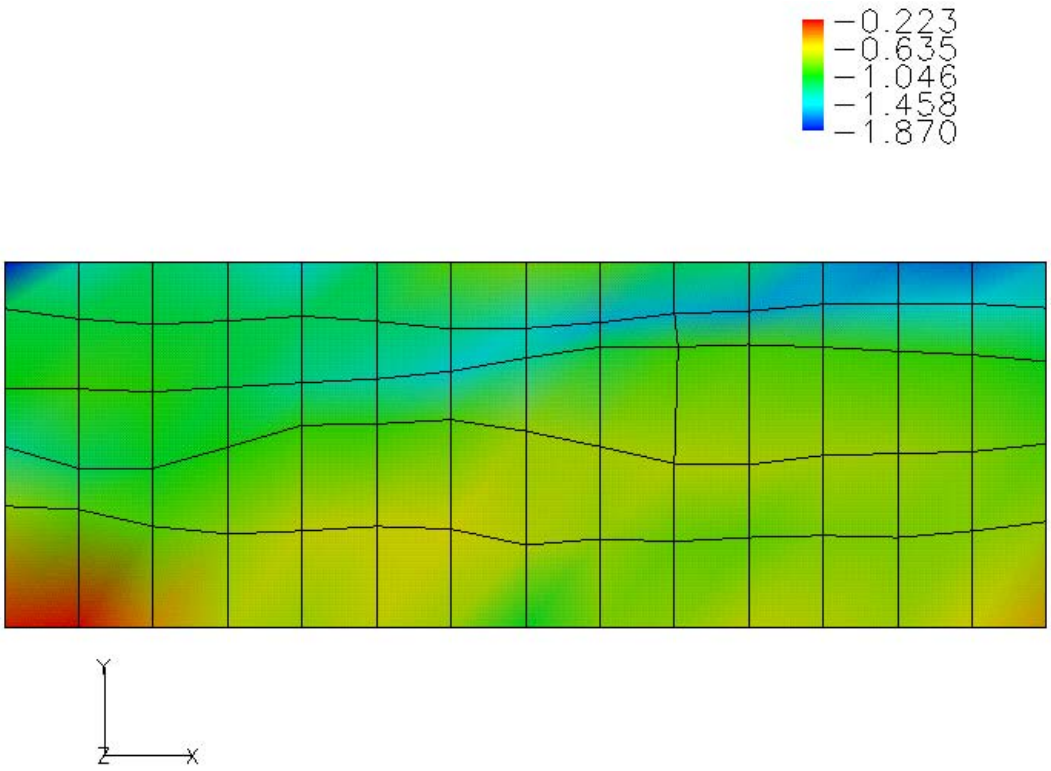

Figure 4.36. Deformed mesh: Coarse fibre test, Y-Y Logarithmic Strain.

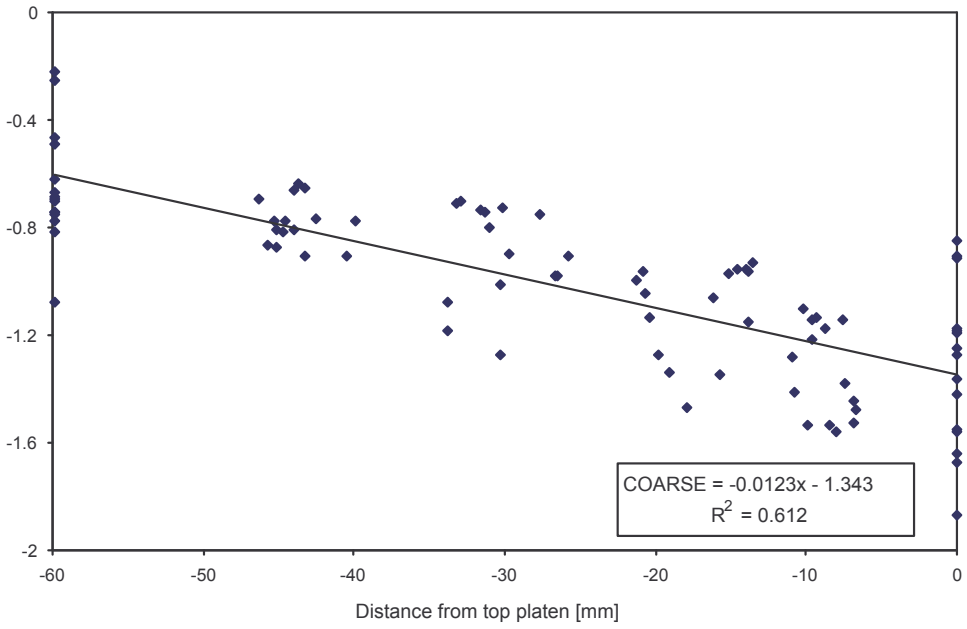

Figure 4.37. Graph showing the Y–Y Logarithmic strain versus sample depth for the coarse fibre test.

4.3 Ancillary grooving study

The image acquisition system and ITA software were also employed in an investigation into the mechanisms governing the dewatering of bagasse during milling (Kauppila et al. 2003). Researchers at James Cook University identified two distinctive modes of blanket failure during uniaxial compression between grooved surfaces (Kauppila et al. 2001(2)). As a result of these findings, the thick blanket uniaxial compression cell used for the investigation was modified to incorporate a viewing window (Figure 4.38), to further assess the blanket failure.

Figure 4.38. Thick blanket uniaxial cell with fitted viewing window.

A subsequent series of experiments were conducted, in which video footage was captured for each sample. Time calibration of the video and load/displacement data, provided a useful tool for assessing the mode and severity of blanket failures, and the load required to cause failure. Furthermore, interesting observations were made in regard to the initiation of local juice saturation within the blanket, which provided some insight into the juice flow through the samples. Figure 4.39 shows the initiation of juice saturation in the material adjacent to the groove tips, for a prepared cane experiment involving 50 mm/55° grooves.

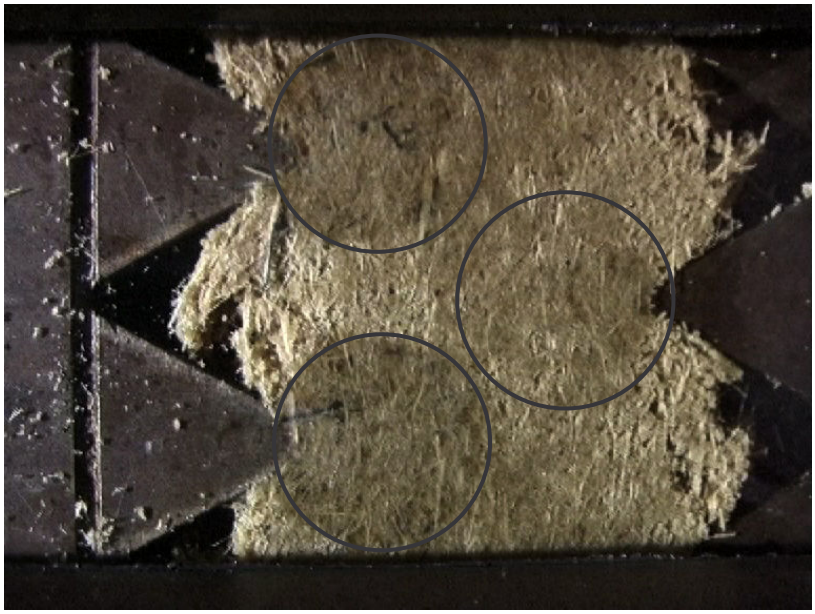

Figure 4.39. Image showing the initiation of juice saturation in the material adjacent to the groove tips.

The ITA software was applied to the image series' from suitable experiments, with the aim of gaining further insight into the development of juice flow through the blanket, via ITA deformation results. In most cases, the large displacements applied to the samples, combined with the smaller viewing window (120 mm by 90 mm) and the discrete nature of the material/groove interactions, caused excessive local mesh distortions. Hence, nodal singularities in the ITA results were observed. However, qualitatively, the results provided significant insight into the development of pressure within the blanket, via animation of the fibre strain field. The initial image showing the grooves and the visible section of the blanket for a large mass prepared cane experiment is shown in Figure 4.40.

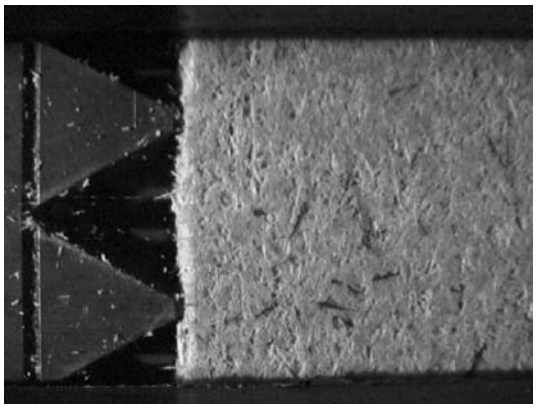

Figure 4.40. Image from a uniaxial grooving experiment with 50 mm/55° grooves.

The deformed mesh for selected times in the ITA analysis of the sample shown are displayed in Figure 4.41. The contoured variable is the local void ratio, defined as the volume of voids divided by the volume of fibre.

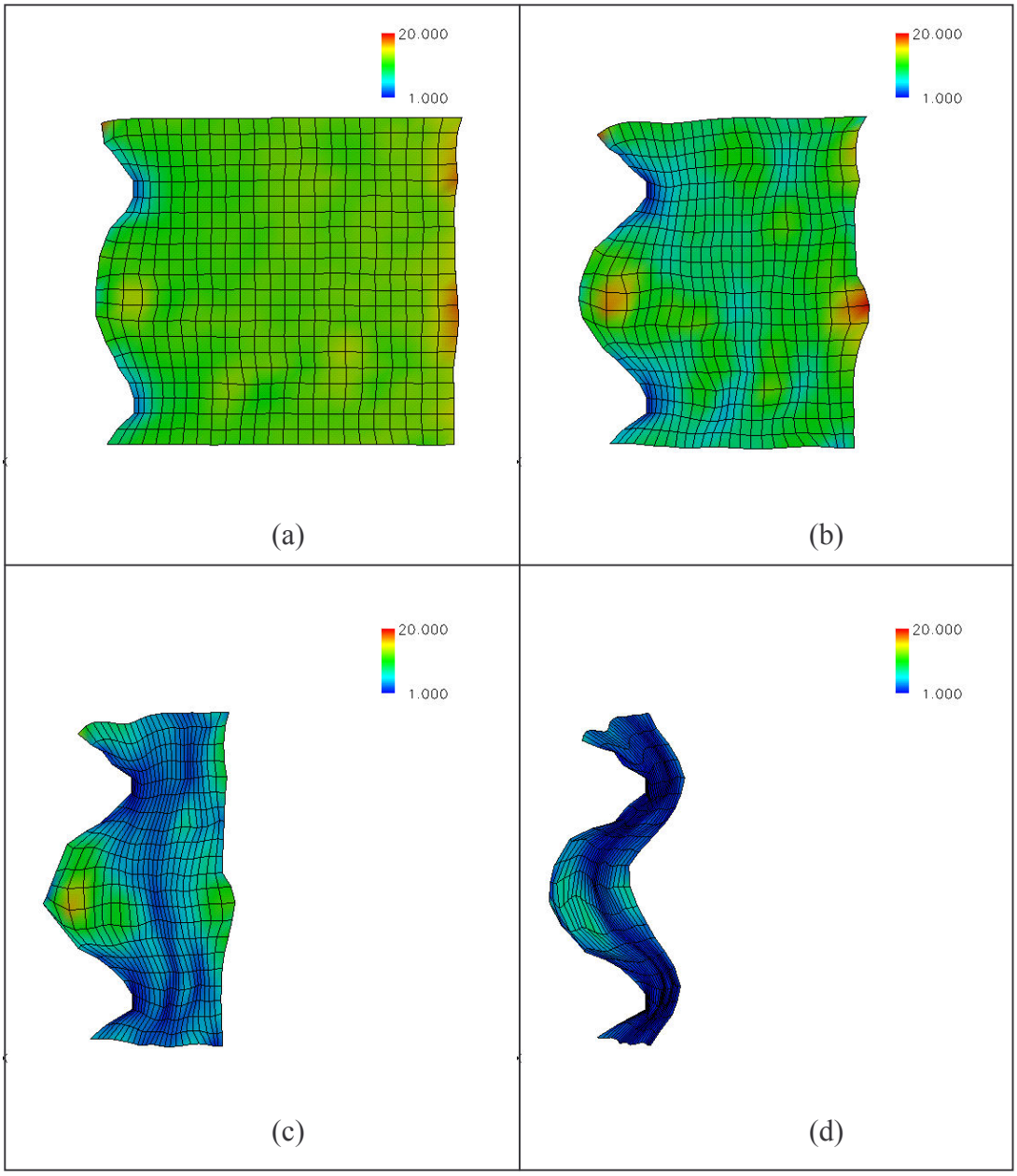

Figure 4.41. Selected frames from a void ratio animation of a uniaxial grooving experiment with 50 mm/55° grooves.

As the blanket starts to deform (Figure 4.41(a)), regions of high pressure (low void) develop in the material adjacent to the groove tips. Material near the blanket surface begins to fold into the groove, producing a region of tensile strain (or high void) in

the material entering the groove void. As the influence of the mating groove on the opposite platen increases (Figure 4.41(b)), the folding is seen to become more prominent. As a result of this influence, the magnitude of the void ratio in the groove increases further, producing a strong pressure gradient between the highly deformed material at the groove tips and the low–pressure region in the groove void. As the deformation increases (Figure 4.41(c)), a strong 'bridge' of highly compacted material develops about the centre–line of the sample, which acts to inhibit further folding of blanket into the groove. If this bridge is sufficiently strong, folding of the blanket into the grooves will cease, and the tips of the grooves will begin cutting into the blanket surface. The low-pressure region of material in the base of the groove is seen to exist throughout the remaining duration of compression (Figure 4.41(d)). The results thus infer that juice flow initiates at the groove tips, and flows into the low–pressure region of the groove void, or back into the sample. Then, as overall deformation increases, the juice is forced out of the sample through the low–pressure material in the grooves, exiting into the groove until the applied compression ceases. It is noted that the low-pressure regions of material present in the grooves provide paths of low resistance for juice flow through the nip, and are hence likely to contribute to reabsorption.

4.4 Summary

A small series of confined flat–platen uniaxial compression experiments was conducted and the ITA software was calibrated for prepared cane and final bagasse over a wide range of fibre density. Deformation results from the sighting trials identified the inherent difficulty in obtaining both uniform initial sample density and a 'plane strain' scenario for the simple confined uniaxial compression regime. The ITA deformation mappings of the samples showed large variance in strain with no distinctive trend in the direction of compression, as might be expected due to cell wall friction. This behaviour was attributed primarily to sample loading, and pre–compression in the same direction as the experiment compression. Furthermore, the presence of large material particles within samples of both materials was hypothesised to contribute to the erratic nature of the local material motion during compression. The need for repetitive experiments was also identified as a means to assess the repeatability of measured deformations.

The uniaxial cell depth was reduced from 98 mm to 25 mm in order to restrict material motion perpendicular to the two–dimensional viewing plane, thus more closely approaching a plane–strain scenario. A new method involving loading the samples into the cell and pre–compressing perpendicular to the direction of the experiment compression was implemented; with the aim to achieve more uniform initial sample density. A fines material was manufactured by sieving the finer particles from final bagasse, with a view to showing a reduction in deformation variance with the exclusion of larger bagasse particles. The auxiliary trials were thus conducted with the above testing modifications in place. Deformation results for final bagasse showed a repeatable trend in deformation in the direction of compression. However, local variations in the deformation data across the width were still evident due to the influence of the larger bagasse particles within each sample. The deformation results for the fines material showed a similar, yet stronger, trend in deformation in the direction of compression. Variations in the strain across the sample width were significantly reduced with the omittance of the larger bagasse particles, hence proving their contribution to variance in sample deformations. The cell modifications produced significantly improved the initial sample homogeneity and the planar nature of the sample strain. However, for a material such as final bagasse, the presence of a large fibre size distribution infers an inherent difficulty in obtaining plane–strain conditions.

The ancillary application of the image acquisition system and ITA software to determining the failure mode of prepared cane and bagasse blankets during uniaxial compression between grooved surfaces was also presented, identifying the role played by the ITA software in this investigation. Insight was gained into juice flow through the blanket and probable contributions to reabsorption.